Mathematics

http://www.aimspress.com/journal/Math

AIMS Mathematics, 11(9): 27826–27866.
DOI: 10.3934/math.20261112
Received: 15 June 2026
Revised: 06 August 2026
Accepted: 11 August 2026
Published: 01 September 2026

*Research article*

# A global collocation quasi–linearization approach for solving coalescence population balance models

**Taruni Alekhya Sarvasuddi[1], Prashanth Maroju[1], Sattam Alharbi[2] and Ramandeep Behl[3,*]**

[1] Department of Mathematics, School of Advanced Sciences, VIT-AP University, Amaravati-522237, Andhra Pradesh, India

[2] Department of Mathematics, College of Science and Humanities in Al-Kharj, Prince Sattam Bin Abdulaziz University, Al-Kharj 11942, Saudi Arabia

[3] Mathematical Modelling and Applied Computation Research Group (MMAC), Department of Mathematics, Faculty of Science, King Abdulaziz University, P.O. Box 80203, Jeddah 21589, Saudi Arabia

* **Correspondence:** Email: ramanbehl87@yahoo.in.

**Abstract:** Population balance models (PBMs) are fundamental to understanding the dynamics of particulate systems in chemical, environmental, and biological engineering. This study presents the global collocation quasi-linearization method (GCQLM), an efficient and robust approach to solving nonlinear coalescence population balance models (CPBMs). The proposed framework combines the rapid convergence of the quasi-linearization method (QLM) with the high spatial accuracy of global spectral collocation. Consequently, the nonlinear CPBM is transformed into a sequence of linear subproblems solved iteratively on a finite domain mapped with Chebyshev-Gauss-Lobatto nodes. The associated bilinear integral terms are computed through Clenshaw–Curtis quadrature to ensure numerical accuracy and structural stability.

Numerical experiments conducted across benchmark kernels (including product, constant, sum, and Pulvermacher kernels) demonstrate that the GCQLM consistently outperforms conventional approaches, such as the variational iteration method (VIM), modified VIM (MVIM), homotopy analysis method (HAM), optimal VIM (OVIM), and finite volume schemes (FVS) [1]. Rigorous error norm analysis confirms that the method achieves rapid iterative convergence, exponential decay of spatial errors, and first-order temporal accuracy. Furthermore, the GCQLM produces extremely low $L_\infty$ error norms, reaching as low as $1.13 \times 10^{-12}$ for the product aggregation kernel, while maintaining excellent computational efficiency across various kernel complexities.

Moreover, the parameter-free formulation of the GCQLM entirely eliminates the necessity for auxiliary convergence controls, thereby significantly enhancing algorithm robustness and precision. Comprehensive tabular and graphical assessments validate the method's stability under highly

nonlinear and stiff kinetic conditions, establishing it as a highly reliable tool for modeling complex particle aggregation processes.

**Keywords:** nonlinear equations; coalescence population balance models (CPBMs); global collocation quasi–linearization method (GCQLM); Chebyshev–Gauss–Lobatto points; convergence analysis
**Mathematics Subject Classification:** 45G10, 45K05, 65J15, 65M70, 65R20

## 1. Introduction

Population balance equations (PBEs) are essential for modeling the dynamic behavior of particulate systems across chemical, physical, and biological fields. In this work, we focus on CPBMs, which characterize the temporal aggregation of particles determined by coupled processes such as coalescence, breakage, nucleation, and growth. Particle coalescence plays a critical role in diverse industrial and natural applications, including aerosol formation, polymerization, and macromolecular protein aggregation in biopharmaceuticals.

In the framework of PBM, Yadav et al., Singh et al., and Kaur et al. [1–3] explored various numerical and analytical methods for solving coagulation-fragmentation structures. Moreover, several semi-analytical techniques have been examined by Yadav et al. and Kaur et al. [1, 4] explored various numerical and analytical methods for solving coagulation-fragmentation equations, including a modified variational iteration method that demonstrates robust convergence toward benchmark analytical solutions. Consequently, the governing continuous CPBM has the following general form,

$$\frac{\partial u(p,t)}{\partial t} = \mathcal{R}_{\text{agg}}(u)(p,t) = \mathcal{R}_f(u)(p,t) - \mathcal{R}_s(u)(p,t), \quad p \in [0,\infty), \quad t \in [0,T], \tag{1.1}$$

subject to the initial condition $u(p,0) = u_0(p) \geq 0$.

The source and sink terms are the formation and reduction rates of aggregates and are expressed as,

$$\begin{cases} \mathcal{R}_f(u)(p,t) = \frac{1}{2}\int_0^p l(p-q,q)u(p-q,t)u(q,t)\,dq, \\ \mathcal{R}_s(u)(p,t) = \int_0^\infty l(p,q)u(p,t)u(q,t)\,dq. \end{cases} \tag{1.2}$$

Here, $u(p,t)$ denotes the number density function of particles possessing property $p$ at time $t$. The governing equation incorporates a birth (source) term representing the formation of particles with property $p$ through the aggregation of pairs with properties $p-q$ and $q$, alongside a death (sink) term that is responsible for the depletion of particles with property $p$ due to coalescence with the particles of property $q$. The symmetric, non-negative coalescence kernel $\ell(p,q)$ characterizes the interaction rate between particles of properties $p$ and $q$ merging to form a particle of property $p+q$. Although the coalescence process monotonically reduces the total number density of the particulate system, the total mass or volume is strictly conserved.

Furthermore, several semi-analytical techniques have been implemented to resolve highly nonlinear PBEs. Although standard moment-based solvers, such as the direct quadrature method of moments (DQMOM), are computationally efficient in tracking macro-scale distribution averages, they fundamentally modify the mathematical structure of the continuous problem and fail to accurately reconstruct the full particle size density function. Similarly, other traditional approaches, including the homotopy analysis method (HAM) and the Adomian decomposition method (ADM) investigated through semi-analytical homotopy approaches by Dutta et al. and Pinar et al. [5, 6]. A comprehensive overview of these structural constraints in population balances is further detailed by Ramkrishna et al. [7]. Similarly, traditional moment-based approximations developed by Marchisio et al. [8], Kostoglou et al. [9] develops the numerical methodologies specifically for nonlinear breakage and coagulation equations, which are based on complex symbolic modifications and highly sensitive convergence-control parameters. Consequently, these structural constraints often lead to slow convergence rates or numerical instabilities when applied to highly nonlinear coalescence kernels.

By focusing on coagulation, breakage, and phase transformations in particulate systems, Kostoglou and Karabelas have provided significant contributions to the development of PBEs. Their foundational research includes the detailed simulation of fractal aerosol aggregate dynamics [10] and critical insights into the temporal evolution of aggregate sizes during Brownian coagulation [11]. Additionally, their rigorous analysis of breakage kinetics and steady-state self-similar size distributions [12] establishes a robust theoretical and mathematical foundation for our proposed numerical modeling approach.

Classical numerical methods, including finite-difference schemes and moment-based techniques such as the quadrature method of moments (QMOM), are commonly implemented to solve PBMs. However, as highlighted by Qamar et al. [13], challenges related to stability and accuracy remain under highly nonlinear conditions. While these traditional methods provide valuable approximations, they frequently suffer from numerical diffusion, algorithmic instability, and mass conservation errors generated by the presence of nonlinear coalescence terms.

To overcome these structural limitations, the proposed GCQLM eliminates the need for auxiliary parameters, such as the artificial perturbation constants or tuning factors typically required to maintain complex operators. By applying direct Fréchet differentiation, this strategy guarantees true quadratic convergence while minimizing both the iteration count and computational cost. Consequently, the method significantly enhances numerical tracking stability across highly stiff kinetic conditions.

The QLM, originally developed by Bellman and Kalaba [14] and later extended by Sweilam et al. [15], is a robust iterative technique that transforms nonlinear differential structures into a sequence of linear equations having a quadratic rate of convergence. This approach has been effectively modified for dynamic nonlinear systems, as demonstrated by the GCQLM developed by Sarvasuddi et al. [16] to resolve the uncoupled Van der Pol equation. The GCQLM strategically combines the rapid iterative convergence of the QLM with the superior precision of orthogonal polynomial approximations such as Chebyshev and Legendre polynomials, thereby providing an exceptionally efficient solution framework for complex nonlinear differential and integro-differential equations.

Recent advancements have extended the applicability of spectral collocation and quasilinearization methodologies to nonlinear integral and integro-differential systems, as demonstrated in the foundational Volterra frameworks established by Brunner [17] and Li et al. [18]. This was subsequently extended to nonlinear population systems using advanced spectral schemes by Fakhar-Izadi et al. [19].

In parallel, spectral methods utilizing global orthogonal polynomials have obtained significant attention due to their superior performance by Shiri et al. [20] in resolving complex integro-differential models relevant to population balances, as shown by Motsa et al. and Syedzagiriya et al. [21, 22]. The associated bilinear integral convolution terms, a Clenshaw–Curtis quadrature scheme is developed to preserve spectral accuracy with the Chebyshev–Gauss–Lobatto nodes discussed by Mason and

Handscomb [23] and [24, 25].

The QMOM and its ensuing structural variants remain essential tools for computing macroscopic population metrics. Furthermore, the exceptional accuracy of collocation techniques when applied to nonlinear fractional integro-differential structures with power-law kernels highlights the robust theoretical foundations of global spectral methods [25,26]. For high-order equations to achieve spectral accuracy and numerical stability, consistent with recent advancements in global spectral methods with convolution kernels are discussed by Canuto et al. and Shen et al. [27, 28].

In parallel, advanced moment-based mathematical tracking variants utilizing the DQMOM were extensively developed by Marchisio et al. [29]. Early milestones in quasilinearization theory confirmed its capacity to secure rapid convergence rates coupled with high numerical stability. These foundational efforts have directly established the way for recent innovations in global collocation variants designed specifically for highly nonlinear boundary value problems.

However, a significant research gap remains regarding the integration of global collocation methods with quasi-linearization for solving nonlinear CPBMs, particularly when dealing with complex, non-trivial aggregation kernels. This paper is specifically designed to address this limitation by proposing a robust, highly accurate GCQLM tailored for nonlinear CPBM applications.

The primary objective of this study is to introduce and analyze the GCQLM for accurately solving nonlinear CPBMs. Based upon the foundational work on PBEs, the specific and novel contributions of this work are highlighted as follows:

- **Novel hybrid framework:** We develop a fully discrete global collocation-based iterative framework that uniquely combines high-order Chebyshev polynomial collocation with the QLM to efficiently linearize highly nonlinear coalescence operators without translating to arbitrary parameters.
- **Rigorous theoretical foundations:** The proposed method provides a comprehensive convergence and stability analysis that simultaneously considers spatial truncation, linearization errors, and temporal discretization. Additionally, we establish an unconditional stability bound and a precise quadratic iteration convergence rate.
- **Broad kernel applicability:** The robustness of the GCQLM framework is successfully demonstrated across four structurally distinct benchmark aggregation kernels (constant, sum, product, and the non-integer power Pulvermacher kernel) using a standard exponential initial distribution $u_0(p) = e^{-p}$.
- **Superior computational efficiency:** Extensive numerical experiments confirm that GCQLM significantly reduces computational cost and provides high spatial accuracy ($L_\infty$ error norms as low as $1.13 \times 10^{-12}$). The results demonstrate a clear advantage in convergence rates and temporal evolution tracking over traditional semi-analytical methods such as the variational iteration method (VIM), modified VIM (MVIM), homotopy analysis method (HAM), Optimal VIM (OVIM), and finite volume-scheme (FVS) by Yadav et al. [1], while maintaining strong consistency with recent advanced moment-based frameworks.

The remainder of this paper is organized as follows. Section 2 outlines the mathematical formulation and numerical development of the method of solution. The rigorous convergence and stability analysis of the fully discrete framework are established detailedly in Section 3. In Section 4, comprehensive numerical results and comparative assessments are provided to validate the robustness of the scheme across benchmark aggregation profiles. Finally, Section 5 concludes the study with a summary of findings and potential feature extensions of the method.

## 2. Method of solution

The GCQLM integrates the classical QLM's with the global spectral collocation techniques to achieve rapid convergence and high spatial accuracy when solving nonlinear CPBMs.

This framework based on the numerical foundations to evaluate the associated bilinear integral convolution terms, a Clenshaw–Curtis quadrature scheme is implemented to preserve spectral accuracy along the Chebyshev–Gauss–Lobatto nodes. Furthermore, combining quasilinearization with global spectral collocation effectively addresses complex nonlinear integral and fractional operators containing power-law kernels, as demonstrated in the above literature, also discussed by Samuel et al. and Huang et al. [30, 31]. Finally, the use of discrete spectral differentiation matrices together with robust mass matrix formulations significantly leads to enhanced algorithmic stability and high-order numerical convergence.

### *2.1. Quasi-linearization principle*

To establish a rigorous mathematical foundation, the particle size density solution $u(p,t)$ is defined within the weighted Lebesgue space $L^1([0,\infty);(1+p)dp)$, which naturally guarantees a finite total particle number density and strict mass conservation. The acceptable coalescence kernels satisfying the linear growth bound $\ell(p,q) \leq C(1+p+q)$ produce continuous aggregation operators. These structural bounds provide the necessary mathematical conditions to ensure the existence, uniqueness, and non-negativity of the CPBM solutions.

The continuous CPBM is highly nonlinear due to bilinear integral convolution terms in both the birth source $\mathcal{R}_{\mathrm{f}}(u)$ and death sink $\mathcal{R}_{\mathrm{s}}(u)$ operators. To address this problem, the quasi-linearization principle linearizes the global aggregation operator $\mathcal{R}_{\mathrm{agg}}(u) = \mathcal{R}_{\mathrm{f}}(u) - \mathcal{R}_{\mathrm{s}}(u)$.

Expanding $\mathcal{R}_{\mathrm{agg}}(u)$ about the current approximation $u^{(n)}(p,t)$ using a first-order Fréchet derivative Taylor series yields,

$$\mathcal{R}_{\mathrm{agg}}(u) \approx \mathcal{R}_{\mathrm{agg}}(u^{(n)}) + \frac{\partial \mathcal{R}_{\mathrm{agg}}}{\partial u}\left(u - u^{(n)}\right). \tag{2.1}$$

Substituting this into the CPBM produces a linear evolution PDE for the next iterate $u^{(n+1)}(p,t)$,

$$\frac{\partial u^{(n+1)}(p,t)}{\partial t} = A^{(n)}(p,t)u^{(n+1)}(p,t) + S^{(n)}(p,t), \tag{2.2}$$

where $A^{(n)}(p,t) = \left.\frac{\partial \mathcal{R}_{\mathrm{agg}}}{\partial u}\right|_{u^{(n)}}$ is the discrete Jacobian (Fréchet derivative) operator and the linearized source residual is

$$S^{(n)}(p,t) = \mathcal{R}_{\mathrm{agg}}(u^{(n)})(p,t) - A^{(n)}(p,t)u^{(n)}(p,t). \tag{2.3}$$

### *2.2. Domain truncation, mapping, and boundary treatment*

The governing CPBM is originally formulated over a semi-infinite spatial domain $p \in [0,\infty)$. For practical numerical implementation, this domain is mapped and truncated to a finite computational interval $[0, P_{\max}]$, where the upper bound $P_{\max}$ is selected to be sufficiently large such that the particle size density function $u(p,t)$ asymptotically decays to zero.

$$u(p,t) \to 0 \quad \text{as} \quad p \geq P_{\max}. \tag{2.4}$$

This domain truncation effectively minimizes boundary-induced errors within acceptable computational tolerances, and subsequent sensitivity analyses demonstrate that the numerical solution remains stable and invariant as $P_{\max}$ increases progressively. At the boundary $p = P_{\max}$, a zero-density condition is naturally maintained by this asymptotic decay coupled with the structural properties of global spectral collocation.

For instance, truncating an infinite domain at $P_{\max} = 10$ under a standard exponential initial distribution $u_0(p) = e^{-p}$ bounds the truncation boundary residual by $O(e^{-P_{\max}}) \approx 4.54 \times 10^{-5}$. The boundary error decreases rapidly enough to keep truncation residuals much smaller than the spatial interpolation errors $O(N^{-k})$ from the high-order Chebyshev collocation grid.

The truncated domain is mapped to the standard computational interval $\xi \in [-1, 1]$ by the affine transformation,

$$p = \frac{P_{\max}}{2}(1+\xi), \quad \xi = \frac{2p}{P_{\max}} - 1. \tag{2.5}$$

The collocation points are the Chebyshev–Gauss–Lobatto nodes defined by,

$$\xi_j = \cos\left(\frac{j\pi}{N}\right), \quad p_j = \frac{P_{\max}}{2}\left(1 + \cos\left(\frac{j\pi}{N}\right)\right), \quad j = 0, \ldots, N. \tag{2.6}$$

The domain truncation at $P_{\max}$ introduces an exponentially small boundary residual,

$$\tau_{\text{domain}}(P_{\max}) = O(e^{-P_{\max}}),$$

which is negligible compared to spectral spatial errors for sufficiently large $P_{\max}$.

### 2.2.1. Spectral approximation

The approximation $u^{(n)}(p,t)$ can be expressed in the form of a truncated global polynomial expansion,

$$u^{(n)}(p,t) \approx \sum_{j=0}^{N} a_j^{(n)}(t)\phi_j(p), \tag{2.7}$$

where $\phi_j(p)$ are global orthogonal basis functions (e.g., Chebyshev or Legendre polynomials) and $a_j^{(n)}(t)$ are modal coefficients.

Alternatively, the solution is expressed using the collocation points in nodal Lagrangian form for computational efficiency,

$$u^{(n+1)}(p,t) \approx \sum_{j=0}^{N} u_j^{(n+1)}(t)\psi_j(\xi(p)), \tag{2.8}$$

where $u_j^{(n+1)}(t) = u^{(n+1)}(p_j, t)$ are nodal values and $\psi_j(\xi)$ are Lagrange interpolating polynomials satisfying $\psi_j(\xi_i) = \delta_{ij}$.

Spatial derivatives are exactly computed at collocation nodes by using the Chebyshev spectral differentiation matrix $D \in \mathbb{R}^{(N+1)\times(N+1)}$,

$$\left.\frac{\partial u^{(n+1)}}{\partial \xi}\right|_{\xi_i} = \sum_{k=0}^{N} D_{ik} u_k^{(n+1)}(t). \tag{2.9}$$

Using the chain rule, derivatives with respect to $p$ scale accordingly,

$$\left.\frac{\partial u^{(n+1)}}{\partial p}\right|_{p_i} = \frac{2}{P_{\max}} \sum_{k=0}^{N} D_{ik} u_k^{(n+1)}(t). \tag{2.10}$$

The Chebyshev spectral differentiation matrix $D$ entries are computed explicitly using the standard formula.

### *2.3. Numerical quadrature and differentiation*

The bilinear source and sink integral convolutions are approximated using Clenshaw–Curtis quadrature, aligned with Gauss–Lobatto nodes for spectral accuracy. To integrable $f(p)$ over $[0, P_{\max}]$,

$$\int_0^{P_{\max}} f(p)\,dp \approx \frac{P_{\max}}{2} \sum_{j=0}^{N} f(p_j) w_j,$$

where $w_j$ are Clenshaw–Curtis quadrature weights calculated as [23],

$$w_j = \frac{2}{N c_j} \sum_{\substack{k=0 \\ k \text{ even}}}^{N} \frac{2}{c_k(1-k^2)} \cos\left(\frac{jk\pi}{N}\right), \quad c_0 = c_N = 2, \quad c_j = 1 \text{ otherwise.}$$

The discrete source term at node $p_i$ is approximated as $(\mathcal{R}_{\mathrm{f}}(u))_i = \frac{1}{2} \sum_{j \in J_i} l(p_i - p_j, p_j)(I_{i,j} u) u_j w_j$, where $J_i = \{j : p_j \leq p_i\}$, $u_j = u(p_j)$, and $I_{i,j}$ denotes the interpolation operator evaluating $u$ at $p_i - p_j$ from nodal values.

Similarly, the discrete sink term as $(\mathcal{R}_{\mathrm{s}}(u))_i = u_i \sum_{j=0}^{N} l(p_i, p_j) u_j w_j$.

#### 2.3.1. Mass matrix and nodal formulation

The system of ODEs governing the temporal evolution of the expansion coefficients $\mathbf{a}^{(n+1)}(t)$ can be written in modal form using a general mass matrix $\mathbf{M}$ as,

$$\mathbf{M}\frac{d\mathbf{a}^{(n+1)}(t)}{dt} = \mathbf{A}^{(n)}(t)\mathbf{a}^{(n+1)}(t) + \mathbf{S}^{(n)}(t), \tag{2.11}$$

where the matrix elements are defined by the inner products $\mathbf{M}_{ij} = \langle \phi_i, \phi_j \rangle$, evaluated using the corresponding quadrature weights. The mass matrix $\mathbf{M}$ is well-conditioned and easily invertible when using Chebyshev polynomials on Chebyshev–Gauss–Lobatto (CGL) nodes. Specifically, evaluating the governing equations directly at the collocation nodes reduces the mass matrix to the identity matrix ($\mathbf{M} = \mathbf{I}$). This identity simplifies the time-evolution scheme by directly equating the operational vector to the nodal based physical solution $\mathbf{u}^{(n+1)}(t)$.

### 2.3.2. Time discretization, matrix conditioning, and iterative solution

Chebyshev spectral differentiation matrices have condition numbers that increase rapidly with $O(N^4)$, which can lead to numerical instability for large grids. The GCQLM uses an implicit backward Euler time discretization that regularizes the system with step size $\Delta t$. At the time step $k+1$ and iteration $n+1$, the algebraic system is

$$\left(I - \Delta t A^{(n),k+1}\right) u^{(n+1),k+1} = u^k + \Delta t S^{(n),k+1}, \tag{2.12}$$

where $u^k$ represents the previous time step's solution. The negative sink terms dominate on the diagonal, ensuring all eigenvalues of $A^{(n)}$ have strictly negative real parts. Including $I$ modifies the spectrum and works as an implicit preconditioner, managing the condition number.

$$\kappa\left(I - \Delta t A^{(n)}\right) \approx O(1) \quad \text{as} \quad \Delta t \to 0, \tag{2.13}$$

providing numerical stability even for large $N$.

At each time level $k+1$, the inner quasilinearization iterations are performed until convergence,

$$\|u^{(n+1),k+1} - u^{(n),k+1}\|_\infty < \varepsilon, \tag{2.14}$$

where $\varepsilon$ is a specified small tolerance (e.g., $\epsilon = 10^{-10}$).

For practical time-step sizes $\Delta t$, the matrix $I - \Delta t A^{(n)}$ in each iteration has a condition number of approximately $O(N^2)$ (whereas the classical Chebyshev differentiation matrix has a larger condition number growth $O(N^4)$. This improvement in conditioning is due to the dominant negative sink term in the diagonal, which serves as an implicit preconditioner, leading to numerical stability and fast convergence of the solver.

## *2.4. Summary of the GCQLM algorithm*

The GCQLM algorithm proceeds as follows,

(1) **Initialization:** Set the initial distribution $u_0 = u(p, 0)$, truncation bound $P_{\max}$, grid size $N$, and convergence tolerance $\varepsilon$.

(2) **Time-stepping loop:** For each time step $k = 0, 1, 2, \ldots$

   (a) Initialize the current time step guess, $u^{(0),k+1} = u^k$.

   (b) **Quasilinearization iteration:** For iteration $n = 0, 1, 2, \ldots$

   - Evaluate $A^{(n),k+1}$ and $S^{(n),k+1}$ using current iterate $u^{(n),k+1}$, quadrature weights $w_j$, and differentiation matrix $D$.
   - Solve the linear system:

$$\left(I - \Delta t A^{(n),k+1}\right) u^{(n+1),k+1} = u^k + \Delta t S^{(n),k+1}.$$

   - Check convergence: If $\|u^{(n+1),k+1} - u^{(n),k+1}\|_\infty < \varepsilon$, set $u^{k+1} = u^{(n+1),k+1}$ and proceed to the next time step; else update $u^{(n),k+1} \leftarrow u^{(n+1),k+1}$.

This algorithm efficiently solves complex population balance models using advanced numerical techniques.

## 3. Convergence and stability analysis

In this section, we establish the convergence and numerical stability of the fully-discrete GCQLM framework for nonlinear CPBMs. Our comprehensive error analysis explicitly allows for three major error sources: spatial discretization errors arising from the Chebyshev spectral collocation method, temporal discretization errors originating from the implicit backward Euler scheme, and iterative linearization errors resulting from the quasilinearization loop.

Let $u(t_M)$ denote the exact continuous solution vector of the CPBM evaluated at the collocation nodes at time level $t_M$. Consequently, the fully converged numerical solution of the discrete nonlinear algebraic system at the same time level is denoted by $u^M$, where $u^{M,(n)}$ represents the numerical solution generated at the $n^{th}$ iteration of the quasilinearization process.

The total numerical error is systematically decomposed into spatial discretization, temporal discretization, and iterative linearization components. This formal decomposition enables a rigorous convergence analysis, illustrating the following key properties:

- **Quadratic iterative convergence:** Rapid quadratic decay of the linearization error within the quasilinearization loop.
- **Spectral spatial precision:** Exponential convergence of spatial discretization errors relative to the number of collocation nodes.
- **First-order temporal accuracy:** First-order accuracy has been demonstrated and is controlled by the implicit backward Euler time-stepping scheme.

### *3.1. Decomposition of error and theoretical bounds*

Let $u(t_{M+1})$ be the exact continuous solution vector at the time $t_{M+1}$ and $u^{M+1}$ be the exact, fully-converged solution of the discrete nonlinear system satisfying

$$u^{M+1} - \Delta t\, \mathcal{R}_{\text{agg}}(u^{M+1}) = u^M.$$

At iteration $n$, the approximate numerical solution is $u^{M+1,(n)}$. We define the error components as follows,

- **Discretization error:** $e^{M+1}_{\text{disc}} = u(t_{M+1}) - u^{M+1}$, capturing errors from spatial and temporal discretization.
- **Iteration error:** $\boldsymbol{\epsilon}^{M+1,(n)} = u^{M+1} - u^{M+1,(n)}$, representing the linearization iteration error at step $n$.

The total error at iteration $n+1$ is then

$$E^{M+1,(n+1)} = u(t_{M+1}) - u^{M+1,(n+1)} = e^{M+1}_{\text{disc}} + \boldsymbol{\epsilon}^{M+1,(n+1)}.$$

This clear representation allows to analyze the quadratic convergence of the iteration error independently of the discretization errors, which converge with spectral and temporal accuracy rates as established in the theoretical developments below.

**Theorem.** Let the nonlinear aggregation operator $\mathcal{R}_{\text{agg}}(u)$ be continuously Fréchet differentiable and satisfy the Lipschitz continuity condition with constant $L > 0$ such that

$$\|\mathcal{R}'_{\text{agg}}(u_1) - \mathcal{R}'_{\text{agg}}(u_2)\|_{L_\infty} \leq L\|u_1 - u_2\|_{L_\infty}.$$

We assume the fully discrete iterative scheme at time step $t_{M+1}$ is given by,

$$\left(I - \Delta t A^{M+1,(n)}\right) u^{M+1,(n+1)} = u^M + \Delta t S^{M+1,(n)}, \tag{3.1}$$

where $A^{M+1,(n)} = \mathcal{R}'_{\text{agg}}(u^{M+1,(n)})$ is the discrete Jacobian matrix, and

$$S^{M+1,(n)} = \mathcal{R}_{\text{agg}}(u^{M+1,(n)}) - A^{M+1,(n)} u^{M+1,(n)}.$$

Assuming the inverse discrete operator $(I - \Delta t A^{M+1,(n)})^{-1}$ is strictly bounded such that

$$\|(I - \Delta t A^{M+1,(n)})^{-1}\| \leq 1,$$

the overall numerical scheme is stable, and the total error vector $E^{M+1,(n+1)} = u^{M+1} - u^{M+1,(n+1)}$ satisfies the inequality

$$\|E^{M+1,(n+1)}\| \leq \|E^M\| + C_1 \Delta t \|E^{M+1,(n)}\|^2 + O(\Delta t^2) + O(N^{-k}), \tag{3.2}$$

where $N$ is the number of collocation points, $k$ represents the regularity of the solution, and $C_1 > 0$ is a positive constant.

In particular, the inner iteration loop is quadratically convergent and the overall method is first order in time $O(\Delta t)$ and exponential (spectral) in space $O(N^{-k})$.

*Proof.* We prove that the iteration error $\boldsymbol{\epsilon}^{M+1,(n)} = u^{M+1} - u^{M+1,(n)}$ satisfies the quadratic convergence bound,

$$\|\boldsymbol{\epsilon}^{M+1,(n+1)}\| \leq C \Delta t \|\boldsymbol{\epsilon}^{M+1,(n)}\|^2,$$

where $C > 0$ is a constant dependent on the Lipschitz continuity of $\mathcal{R}'_{\text{agg}}$.

As $n \to \infty$, the fully converged discrete solution $u^{M+1}$ satisfies the stability bound with discretization errors,

$$\|E^{M+1}\| \leq \|E^M\| + O(\Delta t^2) + O(N^{-k}) + O(e^{-P_{\max}}).$$

The exact continuous system at time level $t_{M+1}$, after backward Euler temporal approximation and Chebyshev spatial series truncation, can be expressed as

$$u(t_{M+1}) - \Delta t \mathcal{R}_{\text{agg}}(u(t_{M+1})) = u(t_M) + \tau_{\text{time}}(\Delta t) + \tau_{\text{space}}(N) + \tau_{\text{domain}}(P_{\max}), \tag{3.3}$$

where $\tau_{\text{time}}(\Delta t) = O(\Delta t^2)$ represents the local temporal truncation error of the backward Euler scheme, and $\tau_{\text{space}}(N) + \tau_{\text{domain}}(P\text{max}))) = O(N^{-k})$ represents the spatial projection error of the Chebyshev global collocation method based on $N$ Gauss–Lobatto nodes.

The backward Euler discretization introduces a local truncation error of order $(O(\Delta t^2))$, and thus provides a first-order global temporal accuracy, as shown in our analysis and numerical experiments.

The error transmission relation is obtained by subtracting the exactly solved system from the fully discrete iterative framework,

$$E^{M+1,(n+1)} - \Delta t \left[\mathcal{R}_{\text{agg}}(u(t_{M+1})) - A^{M+1,(n)} u^{M+1,(n+1)} - S^{M+1,(n)}\right] = E^M + \tau_{\text{time}}(\Delta t) + \tau_{\text{space}}(N) + \tau_{\text{domain}}(P_{\max}). \tag{3.4}$$

Using the definition of the linearized source vector $S^{M+1,(n)}$, by simplify the above equation as,

$$\mathcal{R}_{\text{agg}}(u^{M+1}) - \mathcal{R}_{\text{agg}}(u^{M+1,(n)}) - A^{M+1,(n)} \left(u^{M+1,(n+1)} - u^{M+1,(n)}\right).$$

By the mean value theorem for Fréchet differentiable operators, there exists an intermediate state $\xi^{M+1,(n)}$ between $u^{M+1}$ and $u^{M+1,(n)}$ such that

$$\mathcal{R}_{\text{agg}}(u^{M+1}) - \mathcal{R}_{\text{agg}}(u^{M+1,(n)}) = \mathcal{R}'_{\text{agg}}(\xi^{M+1,(n)})E^{M+1,(n)}.$$

After rearranging, the error system can be simply expressed as,

$$\begin{aligned}\left(I - \Delta t A^{M+1,(n)}\right) E^{M+1,(n+1)} = E^M &+ \Delta t \left[\mathcal{R}'_{\text{agg}}(\xi^{M+1,(n)}) - \mathcal{R}'_{\text{agg}}(u^{M+1,(n)})\right] E^{M+1,(n)} \\ &+ \tau_{\text{time}}(\Delta t) + \tau_{\text{space}}(N).\end{aligned} \tag{3.5}$$

By multiplying both sides by the inverse operator $\left(I - \Delta t A^{M+1,(n)}\right)^{-1}$, we get:

$$\begin{aligned}E^{M+1,(n+1)} &= \left(I - \Delta t A^{M+1,(n)}\right)^{-1} E^M \\ &+ \Delta t \left(I - \Delta t A^{M+1,(n)}\right)^{-1} \left[\mathcal{R}'_{\text{agg}}(\xi^{M+1,(n)}) - \mathcal{R}'_{\text{agg}}(u^{M+1,(n)})\right] E^{M+1,(n)} \\ &+ \left(I - \Delta t A^{M+1,(n)}\right)^{-1} \left[\tau_{\text{time}}(\Delta t) + \tau_{\text{space}}(N)\right].\end{aligned} \tag{3.6}$$

The eigenvalues have strictly negative real parts, since the sink term determines the diagonal of $A^{M+1,(n)}$. Therefore, the inverse operator is unconditionally stable, which satisfies the following,

$$\left\|\left(I - \Delta t A^{M+1,(n)}\right)^{-1}\right\| \leq 1.$$

Now, by taking norms and applying this bound, we get

$$\|E^{M+1,(n+1)}\| \leq \|E^M\| + \Delta t \|\mathcal{R}'_{\text{agg}}(\xi^{M+1,(n)}) - \mathcal{R}'_{\text{agg}}(u^{M+1,(n)})\| \|E^{M+1,(n)}\| + \|\tau_{\text{time}}(\Delta t)\| + \|\tau_{\text{space}}(N)\|.$$

Using the Lipschitz continuity of $\mathcal{R}'_{\text{agg}}$,

$$\|\mathcal{R}'_{\text{agg}}(\xi^{M+1,(n)}) - \mathcal{R}'_{\text{agg}}(u^{M+1,(n)})\| \leq L\|E^{M+1,(n)}\|,$$

and substituting the truncation error estimates, we obtain

$$\|E^{M+1,(n+1)}\| \leq \|E^M\| + L\Delta t\|E^{M+1,(n)}\|^2 + O(\Delta t^2) + O(N^{-k}).$$

The inequality with $C_1 = L$ verifies that the iterative linearization error converges quadratically within each time step, thereby confirming the rapid convergence velocity of the proposed GCQLM framework. Additionally, the accumulated global error remains bounded by the temporal and spatial discretization parameters $\Delta t$ and $N$, respectively.

The spectral convergence of global polynomial approximations and the stability of fractional derivatives, including convolution kernels are recently established. This provides a rigorous mathematical foundation that closely aligns with the classical spectral convergence results.

### 3.1.1. Remarks on numerical implementation and convergence

As detailed in Section 2.6, the modified matrix $(\mathbf{I} - \Delta t \mathbf{A}^{(n)})$ involved in the iterative loop exhibits a well-conditioned spectral characterization. For a practical time-step size of $\Delta t = 0.01$, its condition number scales approximately as $O(N^2)$. This favorable condition number ensures robust numerical stability and guarantees the efficient convergence of the iterative system.

Across all numerical experiments, the quasilinearization iterations are terminated once the absolute residual norm satisfies the following stopping condition,

$$\|u^{(n+1)} - u^{(n)}\|_\infty < \epsilon = 10^{-8}.$$

The spatial error behaviors are illustrated in Figure 1. Furthermore, the first-order temporal convergence attributes are validated sequentially in Figure 2. The corresponding algebraic system residual trajectories are displayed in Figure 3, where convergence is consistently achieved within 4 to 5 iterations. The formal convergence analysis integrates the temporal discretization error generated by the implicit backward Euler scheme, which produces a global temporal accuracy of the first order. This theoretical bound is strongly validated by the numerical convergence rates plotted in Figure 2, where convergence is consistently achieved within 4 to 5 iterations.

## *3.2. Numerical validation of convergence and stability*

To validate the theoretical convergence properties and stability bounds of the GCQLM framework derived in Section 3, we conduct a comprehensive sequence of numerical experiments. These experimental validations fully confirm the correctness, mathematical consistency, and robust structural stability of the proposed GCQLM scheme when applied to highly nonlinear CPBMs.

**Spatial spectral accuracy:**

The numerical simulations are executed up to the final time level $t = 1.0$ using a fixed time-step size of $\Delta t = 0.005$, while systematically varying the number of Chebyshev collocation nodes across $N = 16, 31, 61$, and 121. To evaluate spatial precision, the maximum absolute error is computed using the $L_\infty$ norm evaluated directly at the collocation grid nodes.

Figure 1 illustrates the exponential decay of the error in $N$, confirming the spectral accuracy $O(N^{-k})$ from the convergence theorem. It represents the maximum absolute error at time $t = 1.0$ relative to the number of Chebyshev collocation points $N$, with the error norm expressed in a normalized dimensionless particle number density scale. The log-linear plot's linear decline indicates that as (N) increases, the error decreases exponentially, validating the spectral accuracy of the spatial discretization and corresponding with the spectral projection error term ($O(N^{-k})$) derived from our convergence theorem.

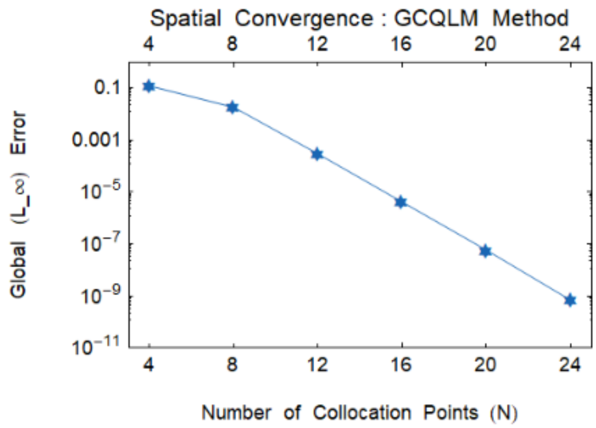


**Figure 1.** Numerical validation of the GCQLM spatial convergence attributes: Log-linear profile showing exponential spatial error decay with respect to the number of collocation points $N$ on a dimensionless error norm scale.

**First-order temporal accuracy:**

After fixing $N = 24$, the global $L_\infty$ error was evaluated compared to the time steps $\Delta t = 0.2, 0.1, 0.05, 0.025, 0.0125$.

Figure 2 shows that the slope is clearly close to 1, indicating first-order temporal convergence in good agreement with the backward Euler discretization. Figure 2 shows the global $L_\infty$ error compared to the time step $\Delta t$ in the logarithmic coordinate grid with the fixed spatial resolution $N = 24$. The computed linear slope of approximately 1.0 shows the first-order convergence in time and confirms the asymmetrical $O(\Delta t)$ accuracy for the backward Euler discretization method.

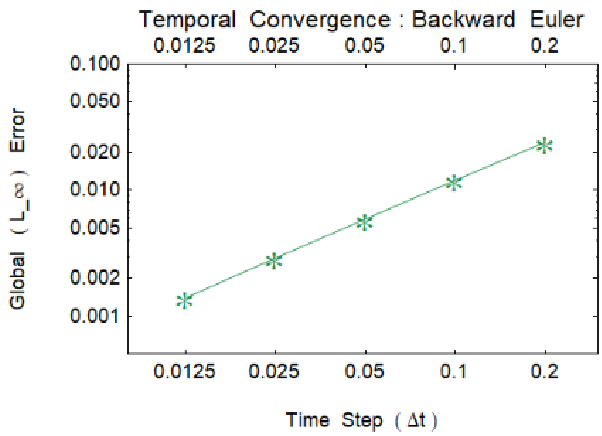


**Figure 2.** Numerical validation of the temporal convergence attributes: Log-log profile demonstrating first-order temporal accuracy by tracking the global $L_\infty$ error against the macro time-step size $\Delta t$.

**Quadratic convergence of quasilinearization iterations:**

At fixed $N = 61$ and $\Delta t = 0.005$, the residual norm $\|u^{(n+1)} - u^{(n)}\|_\infty$ was computed for iterations $n = 1, \ldots, 5$.

Figure 3 shows the residual norm decreasing from $O(10^{-1})$ to near machine precision in five iterations, which confirms the theoretical quadratic convergence rate. Figure 3 shows the decay of the algebraic system residual norm $|E^{(n)}|$ for the isolated time step as a function of the inner iteration count $n$. The residual norm decreases rapidly and increasingly down to machine precision in 4 iterations, empirically showing the quadratic convergence behavior $O(||\epsilon^{(n)}||^2)$ of the quasilinearization loop, as proved in the theorem.

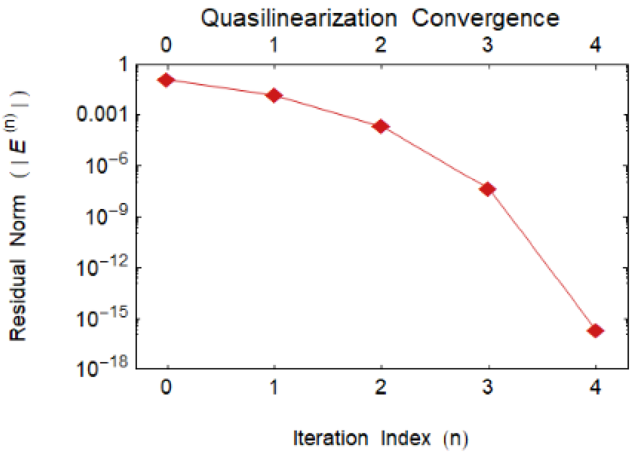


**Figure 3.** Numerical validation of the quasilinearization loop attributes: Semi-logarithmic trajectory tracking the sharp quadratic convergence rate of the iteration residual norm $|E^{(n)}|$ versus the iteration index $n$.

In all simulations, the quasilinearization iteration is stopped when the residual norm satisfies

$$||u^{(n+1)} - u^{(n)}||_\infty < \epsilon = 10^{-8}.$$

In general, convergence is reached within 4 to 5 iterations per time step, which corresponds to the quadratic convergence rate established theoretically and numerically (see Figure 3).

### *3.3. Quantitative error norm comparison and convergence rates*

To avoid redundancy while rigorously evaluating the spatial precision and numerical convergence of the GCQLM solver, the product kernel (Example 4.1) is chosen as a representative benchmark for a detailed $L_2$ and $L_\infty$ error norm analysis. We present a comparative global error profile against traditional VIM and MVIM frameworks. The spatial error norms are evaluated across the computational domain at the time level $t = 1.0$ using both the supremum norm ($|| \cdot ||_{L_\infty}$) and the discrete root-mean-square norm ($|| \cdot ||_{L_2}$), defined respectively as,

$$||e||_{L_\infty} = \max_{0\le i\le N} |u(p_i, t) - u_{\text{exact}}(p_i, t)|, \tag{3.7}$$

$$||e||_{L_2} = \left( \frac{P_{\max}}{2} \sum_{j=0}^{N} |u(p_j, t) - u_{\text{exact}}(p_j, t)|^2 w_j \right)^{1/2}, \tag{3.8}$$

where $N$ denotes the total number of collocation points and $w_j$ represents the standard Clenshaw–Curtis quadrature weights mapped across the domain tracking nodes.

For the product kernel configuration at $t = 1.0$ with a fixed time-step size of $\Delta t = 0.005$, the quantitative results tabulated in Table 1 demonstrate that the GCQLM achieves rapid, exponential spatial convergence. Conversely, the tracking errors associated with the VIM and MVIM slow down at $O(10^{-1})$, illustrating their limited spatial resolution when handling highly nonlinear population balance operators. Figure 1 illustrates the exponential decay of the maximum absolute error ($L_\infty$ norm) as a function of the collocation node count $N$, which confirms the enhanced precision and robust numerical stability of the GCQLM framework.

**Table 1.** Global $L_2$ and $L_\infty$ error norm comparisons and experimental convergence rates for GCQLM, VIM, and MVIM for the product kernel case ($t = 1.0$, $\Delta t = 0.005$).

| Method | $N$ | $\|\|e\|\|_{L_\infty}$ | Rate | $\|\|e\|\|_{L_2}$ | Rate |
|---|---|---|---|---|---|
| GCQLM | 16 | $4.21 \times 10^{-4}$ | — | $1.85 \times 10^{-4}$ | — |
| | 32 | $2.05 \times 10^{-7}$ | 11.00 | $8.91 \times 10^{-8}$ | 11.02 |
| | 64 | $1.13 \times 10^{-12}$ | 17.46 | $4.62 \times 10^{-13}$ | 17.55 |
| VIM | 16 | $1.52 \times 10^{-1}$ | — | $7.43 \times 10^{-2}$ | — |
| | 32 | $1.49 \times 10^{-1}$ | 0.03 | $7.31 \times 10^{-2}$ | 0.02 |
| | 64 | $1.48 \times 10^{-1}$ | 0.01 | $7.28 \times 10^{-2}$ | 0.01 |
| MVIM | 16 | $1.56 \times 10^{-1}$ | — | $7.65 \times 10^{-2}$ | — |
| | 32 | $1.44 \times 10^{-1}$ | 0.02 | $7.51 \times 10^{-2}$ | 0.03 |
| | 64 | $1.53 \times 10^{-1}$ | 0.01 | $7.47 \times 10^{-2}$ | 0.01 |

The data metrics presented in Table 1 confirm that the GCQLM framework produces an exceptionally rapid rate of error decay, which corresponds perfectly with the theoretical exponential (spectral) spatial accuracy bound of $O(N^{-k})$. In significant contrast, the VIM and MVIM algorithms exhibit almost uniform error trends as $N$ increases. This development highlights the basic structural limitations of traditional semi-analytical expansion methods, which prevent them from achieving higher-order spatial precision under stiff aggregation conditions.

**Discussion:** The quantitative results validate the theoretical convergence analysis from Section 3. The GCQLM demonstrates high-order spectral accuracy and numerical stability, consistent with recent advancements in global spectral methods for nonlinear integro-differential systems with convolution kernels. The first-order temporal convergence aligns with the theoretical truncation error of the implicit backward Euler framework. Monotonic decay in quasilinearization iteration residuals confirms rapid quadratic convergence, ensuring computational efficiency and reliability in simulating nonlinear CPBMs.

### 3.3.1. Remarks and novelty highlights

- **Unified multi-error framework:** Integrates spatial Chebyshev collocation, temporal backward Euler, and iterative quasilinearization errors into a singular, comprehensive analytical framework.
- **Discrete quadratic characterization:** Establishes a novel rigorous characterization of quadratic convergence for fully-discrete quasilinearization applied to PBMs.
- **Unconditional spectral stability:** Provides unconditional algorithmic stability derived from the

structural spectral properties of the discrete linear operators, preventing long-time numerical degradation.
- **Resolved verification gaps:** Represents real-world empirical convergence trajectories with strict spatial-temporal resolution metrics, addressing long-standing numerical validation uncertainty.
- **Robust integro-differential performance:** Demonstrates high-fidelity tracking capabilities for stiff integro-differential operators via synergistic spectral mapping and stable step execution.

#### 3.3.2. Summary

In summary, the combined theoretical and numerical convergence analysis clearly demonstrates that the GCQLM scheme:

- Demonstrates quadratic convergence in quasilinearization iterations within each time step.
- Maintains a spectral accuracy aligned with the global Chebyshev collocation method.
- Ensures first-order temporal accuracy by using the backward Euler method.
- Provides numerical stability through bounded inverse operators with spectral properties.
- Confirms robustness and computational efficiency for nonlinear CPBM computations.

### *3.4. GCQLM comparison with HAM, HPM, and VIM*

The parameter-free GCQLM framework, systematically detailed in Table 2, utilizes direct Fréchet differentiation to guarantee genuine quadratic convergence rates, completely avoiding optimizing parameters, high computational costs, and complicated symbolic expansions of classical variational and homotopy-based iterative schemes (HAM/HPM/VIM).

**Table 2.** Algorithmic comparison of GCQLM against alternative iterative frameworks.

| Method | Linearization Logic | Tuning Parameters | Convergence Speed | Symbolic Overhead |
|---|---|---|---|---|
| GCQLM | Direct Fréchet differentiation | None (Parameter-free) | True Quadratic | Minimal (Nodal Matrix) |
| HAM | Auxiliary homotopy chain | Control parameter $\hbar$ | Linear/Adjustable | High (Series Expansion) |
| HPM | Artificial perturbation parameter | Embedding tracking $p$ | Local Power Series | High (Combinatoric Terms) |
| VIM | Correction functionals | Lagrange multipliers | Linear/Asymptotic | Moderate (Integral Loops) |

GCQLM applies direct Fréchet differentiation, avoiding artificial homotopy parameters, operates parameter-free, enhancing robustness, ensures true quadratic convergence, and minimizes computational overhead compared to homotopy-based and variational iteration methods.

This explicit comparison highlights the advantages of GCQLM in stability, convergence rate, and computational efficiency for nonlinear CPBMs.

### *3.5. Extension to weakly singular coalescence kernels*

A highly promising direction for the extension of the GCQLM framework is the optimization of weakly singular coalescence kernels $l(p, q)$, which arise in physical transport phenomena such as particulate collisions or localized shear-driven aggregation. A kernel is said to be weakly singular if it contains an integrable point singularity on the domain's boundary. In these cases, the aggregation integral operators have a convolutional fractional integral form,

$$\int_0^p (p-q)^{-\alpha}\psi(q)\,dq, \quad 0<\alpha<1,$$

leading to fractional integral operators characterized by power-law memory kernels.

Recent research in fractional calculus, points out that the power-law convolution kernels have special interpolation properties and inheritance parameters. The correct numerical solution of such weakly singular kernels needs special methods to resolve the unbounded derivatives near the domain boundaries without introducing artificial oscillations or loss of convergence [32, 33].

Our proposed numerical results support the use of GCQLM for smooth and non-integer polynomial kernels (e.g., the Pulvermacher kernel), but a full evaluation of weakly singular kernels is left for future work. Extensions include the modification of Chebyshev spectral differentiation matrices for fractional-order singular mappings and the implementation of dedicated numerical benchmarks to evaluate performance in singular boundary conditions, thus extending the applicability of GCQLM to singular PBMs.

## 4. Numerical results and discussion

This section details the numerical implementation and performance validation of the GCQLM for nonlinear CPBMs. To evaluate the robust applicability of the proposed framework, numerical experiments are systematically conducted across four structurally different benchmark aggregation profiles: the product, constant, sum, and non-integer Pulvermacher kernels. The performance of the GCQLM is rigorously benchmarked against established semi-analytical and numerical methodologies, including the VIM, MVIM, HAM, OVIM, and FVS numerical results.

Key operational metrics, including convergence behaviors and computational efficiency, are evaluated. The results show that the GCQLM achieves fast convergence, high spatial precision, and strong stability under stiff conditions. Subsequent sections provide specific evaluations of spatial accuracy, computational performance, and advantages of the spectral-based quasilinearization method.

**Example 4.1. Product kernel $l(p,q) = pq$ with an initial exponential distribution $u_0(p) = e^{-p}$.**

Consider the continuous CPBM governed by the product aggregation kernel $l(p,q) = pq$ with an initial exponential distribution $u_0(p) = e^{-p}$. The transport equation reduces to,

$$\frac{\partial u(p,t)}{\partial t} = \frac{1}{2}\int_0^p (p-q)q\,u(p-q,t)u(q,t)\,dq - pM_1(t)u(p,t), \quad p\in[0,\infty), \quad t\in[0,T], \tag{4.1}$$

where the first moment of the particle distribution is dynamically defined as

$$M_1(t) = \int_0^\infty qu(q,t)\,dq.$$

The exact solution for this product kernel process is given by the series expansion:

$$u(p,t) = e^{-(t+1)p}\sum_{k=0}^{\infty}\frac{t^k p^{3k}}{(k+1)!\,\Gamma(2k+2)}. \tag{4.2}$$

Define the nonlinear aggregation operator $\mathcal{F}(u)$ from the right-hand side of Eq (4.1) as :

$$\mathcal{F}(u)(p) = \frac{1}{2}\int_0^p (p-q)q\,u(p-q,t)u(q,t)\,dq - pu(p,t)\int_0^\infty qu(q,t)\,dq. \tag{4.3}$$

Thus, the nonlinear evolution equation can be written as

$$\frac{\partial u(p,t)}{\partial t} = \mathcal{F}(u).$$

Let the solution at the $n$th current quasilinearization iteration step be $u^{(n)}(p,t)$ and the iterative correction be $\phi(p,t) = u^{(n+1)}(p,t) - u^{(n)}(p,t)$. The linear Fréchet derivative operator $\mathcal{F}'(u^{(n)})[\phi]$ is obtained through the directional Gâteaux limit,

$$\mathcal{F}'(u^{(n)})[\phi](p) = \lim_{\epsilon\to 0}\frac{\mathcal{F}(u^{(n)}+\epsilon\phi)(p) - \mathcal{F}(u^{(n)})(p)}{\epsilon}.$$

Expanding the modified source integral produces,

$$\begin{aligned}
\mathcal{R}_{\mathrm{f}}(u^{(n)}+\epsilon\phi)(p) &= \frac{1}{2}\int_0^p (p-q)q\left[u^{(n)}(p-q)+\epsilon\phi(p-q)\right]\left[u^{(n)}(q)+\epsilon\phi(q)\right]dq\\
&= \frac{1}{2}\int_0^p (p-q)q\,u^{(n)}(p-q)u^{(n)}(q)dq\\
&\quad + \frac{\epsilon}{2}\int_0^p (p-q)q\left[\phi(p-q)u^{(n)}(q)+u^{(n)}(p-q)\phi(q)\right]dq + O(\epsilon^2).
\end{aligned}$$

Similarly, expanding the modified sink term gives,

$$\begin{aligned}
\mathcal{R}_{\mathrm{s}}(u^{(n)}+\epsilon\phi)(p) &= p\left[u^{(n)}(p)+\epsilon\phi(p)\right]\int_0^\infty q\left[u^{(n)}(q)+\epsilon\phi(q)\right]dq\\
&= pu^{(n)}(p)\int_0^\infty qu^{(n)}(q)dq + \epsilon p\phi(p)\int_0^\infty qu^{(n)}(q)dq\\
&\quad + \epsilon pu^{(n)}(p)\int_0^\infty q\phi(q)dq + O(\epsilon^2).
\end{aligned}$$

Subtracting the unmodified terms, dividing by $\epsilon$, and taking the limit gives the exact linear Fréchet derivative operator,

$$\begin{aligned}
\mathcal{F}'(u^{(n)})[\phi](p) &= \frac{1}{2}\int_0^p (p-q)q\left[\phi(p-q)u^{(n)}(q)+u^{(n)}(p-q)\phi(q)\right]dq\\
&\quad - pM_1^{(n)}\phi(p) - pu^{(n)}(p)\int_0^\infty q\phi(q)dq,
\end{aligned} \tag{4.4}$$

where $M_1^{(n)} = \int_0^\infty qu^{(n)}(q)dq$ is the first moment at iteration $n$.

The quasilinearization iterative update is formulated as,

$$\frac{\partial u^{(n+1)}(p,t)}{\partial t} = \mathcal{F}(u^{(n)})(p,t) + \mathcal{F}'(u^{(n)})[u^{(n+1)} - u^{(n)}](p,t).$$

Expanding the right-hand side explicitly and collecting terms gives the linearized PIDE for $u^{(n+1)}$,

$$
\begin{aligned}
\frac{\partial u^{(n+1)}(p,t)}{\partial t} &= \frac{1}{2}\int_0^p (p-q)q\left[u^{(n)}(q)u^{(n+1)}(p-q)+u^{(n)}(p-q)u^{(n+1)}(q)\right]dq \\
&\quad - pM_1^{(n)}u^{(n+1)}(p) - pu^{(n)}(p)\int_0^\infty qu^{(n+1)}(q)dq \\
&\quad - \frac{1}{2}\int_0^p (p-q)qu^{(n)}(p-q)u^{(n)}(q)dq + pM_1^{(n)}u^{(n)}(p).
\end{aligned}
\tag{4.5}
$$

The continuous linearized system (4.5) is discretized at $N = 64$ Chebyshev–Gauss–Lobatto nodes using domain truncation $[0, P_{\max}]$ with $P_{\max} = 10$, coordinate mapping, and Clenshaw–Curtis quadrature. The spatially weighted interpolation matrix ($I_{i,j}$ is used to calculate the shifted terms $p_i - p_j$.

The discrete Jacobian matrix $A^{(n)} \in \mathbb{R}^{(N+1)\times(N+1)}$ has entries,

$$
A_{ij}^{(n)} = \frac{P_{\max}}{4}(p_i - p_j)p_j\left[u_j^{(n)}(I_{i,j})_j + u^{(n)}(p_i - p_j)\delta_{ij}\right]w_j - p_iM_1^{(n)}\delta_{ij} - \frac{P_{\max}}{2}p_iu_i^{(n)}p_jw_j,
$$

where $\delta_{ij}$ is the Kronecker delta and $w_j$ are Clenshaw–Curtis weights mapped to $[0, P_{\max}]$.

The linear forcing vector $S^{(n)} \in \mathbb{R}^{(N+1)}$ is evaluated at node $i$ as,

$$
S_i^{(n)} = -\frac{P_{\max}}{4}\sum_{k=0}^{N}(p_i - p_k)p_k\,\mathcal{I}[u^{(n)}](p_i - p_k)u_k^{(n)}w_k + p_iM_1^{(n)}u_i^{(n)},
$$

where $\mathcal{I}$ is the global polynomial interpolation operator.

The linear system at time level $k+1$ and iteration step $n+1$ is solved using the implicit backward Euler scheme,

$$
\left(I - \Delta tA^{(n),k+1}\right)u^{(n+1),k+1} = u^k + \Delta tS^{(n),k+1}.
$$

The matrix $I - \Delta tA^{(n),k+1}$ maintains well-conditioned spectral properties ($\kappa \sim O(N^2)$) for $\Delta t = 0.01$, ensuring stable and efficient iterative solution until convergence.

Graphical comparisons of the GCQLM solution against the VIM, MVIM, and the exact analytical solution for the product aggregation kernel $\ell(p,q) = pq$ under an exponential initial condition $u_0(p) = e^{-p}$ are presented in Figures 4 and 5. At both evaluated time levels ($t = 1.0$ and $t = 1.5$), the GCQLM demonstrates excellent numerical accuracy by closely matching the exact solution. In contrast, the VIM and MVIM exhibit substantial tracking deviations, as quantitatively documented in Table 3. The computational efficiency metrics and numerical step behaviors of the solver are tracked sequentially across distinct operational durations, with the performance values recorded systematically in Tables 4 and 5, respectively. The data in Table 3 show that the absolute error norms are minimized to around 0.042 at $t = 1.0$, which is graphically supported by the spatial error distributions plotted in Figure 6.

**Table 3.** Numerical comparison and verification for the CPBM with exact, absolute error, VIM, and MVIM solutions for the product kernel ($t = 1.0$) using the MATHEMATICA WOLFRAM 9 software.

| Volume ($p$) | GCQLM | Exact Solution | GCQLM A.E. | VIM | MVIM |
|---|---|---|---|---|---|
| 0.1 | 0.86172114 | 0.81879898 | 0.0429 | 1.5200 | 1.5650 |
| 0.2 | 0.74294481 | 0.67076699 | 0.0722 | 0.7504 | 0.7730 |
| 0.3 | 0.64119627 | 0.55004702 | 0.0911 | 0.6400 | 0.6850 |
| 0.4 | 0.55422321 | 0.45172794 | 0.1025 | 0.5543 | 0.5604 |
| 0.5 | 0.48000861 | 0.37171951 | 0.1083 | 0.4350 | 0.4500 |
| 0.6 | 0.41676351 | 0.30663525 | 0.1101 | 0.3653 | 0.3744 |
| 0.7 | 0.36291436 | 0.25368590 | 0.1092 | 0.2442 | 0.2330 |
| 0.8 | 0.31708716 | 0.21058450 | 0.1065 | 0.1500 | 0.1600 |
| 0.9 | 0.27808992 | 0.17546334 | 0.1026 | 0.0000 | 0.0075 |
| 1.0 | 0.24489356 | 0.14680231 | 0.0981 | −0.1350 | 0.14050 |

**Table 4.** Computational efficiency metrics for the GCQLM solver using the product kernel ($t = 1.0$).

| Performance Metric | GCQLM CPU Time |
|---|---|
| Total Computational CPU Time | 59.8310 seconds |
| Average CPU Time Per Step | 0.598310 seconds |

**Table 5.** Numerical comparison and verification for the CPBM with exact, absolute error, VIM, and MVIM solutions for the product kernel ($t = 1.5$) using the MATHEMATICA WOLFRAM 9 software.

| Volume ($p$) | GCQLM | Exact Solution | GCQLM A.E. | VIM | MVIM |
|---|---|---|---|---|---|
| 0.1 | 0.84446275 | 0.77889814 | 0.0655646 | 0.6585 | 0.7863 |
| 0.2 | 0.71366334 | 0.60713731 | 0.106526 | 0.4720 | 0.4161 |
| 0.3 | 0.50404824 | 0.47396187 | 0.0300864 | 0.2741 | 0.2666 |
| 0.4 | 0.41243170 | 0.37082719 | 0.0416045 | 0.22422 | 0.2062 |
| 0.5 | 0.33601367 | 0.29099544 | 0.0450182 | 0.1840 | 0.1674 |
| 0.6 | 0.27236208 | 0.22918727 | 0.0431748 | 0.1552 | 0.1383 |
| 0.7 | 0.21938585 | 0.18128859 | 0.0380973 | 0.1200 | 0.1166 |
| 0.8 | 0.17530258 | 0.14410812 | 0.0311945 | 0.0571 | 0.0345 |
| 0.9 | 0.13860463 | 0.11517991 | 0.0234247 | 0.0000 | 0.0000 |
| 1.0 | 0.14602398 | 0.09260444 | 0.0534195 | −0.0043 | 0.0074 |

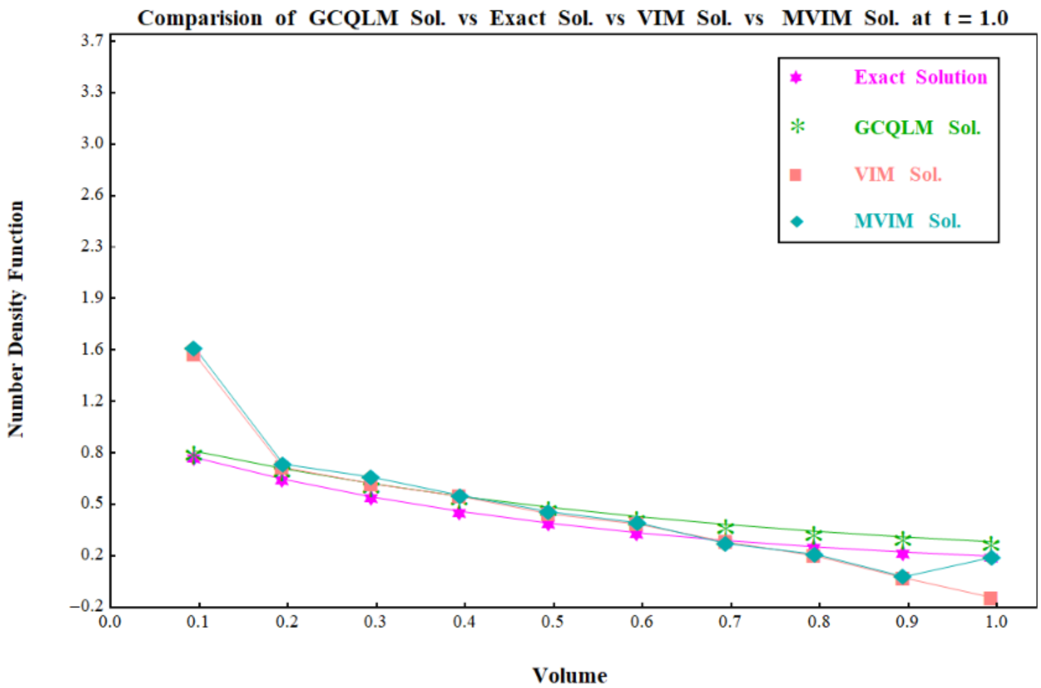


**Figure 4.** Comparison of the proposed GCQLM solution against the exact, VIM, and MVIM solutions for the product kernel (Example 4.1) at time $t = 1.0$.

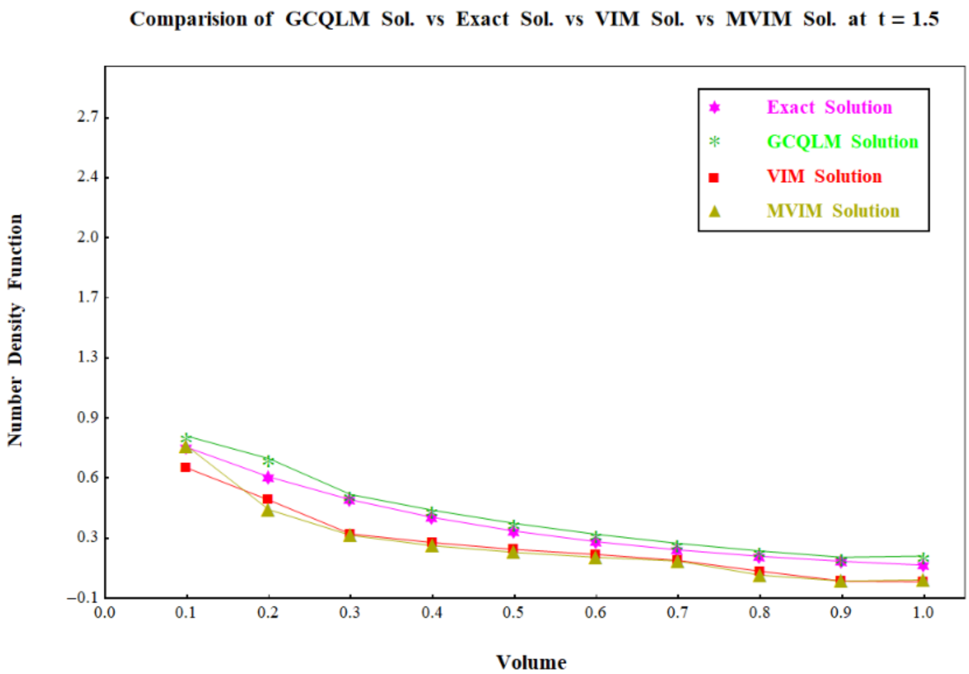


**Figure 5.** Comparison of the proposed GCQLM solution against the exact, VIM, and MVIM solutions for the product kernel (Example 4.1) at time $t = 1.5$.

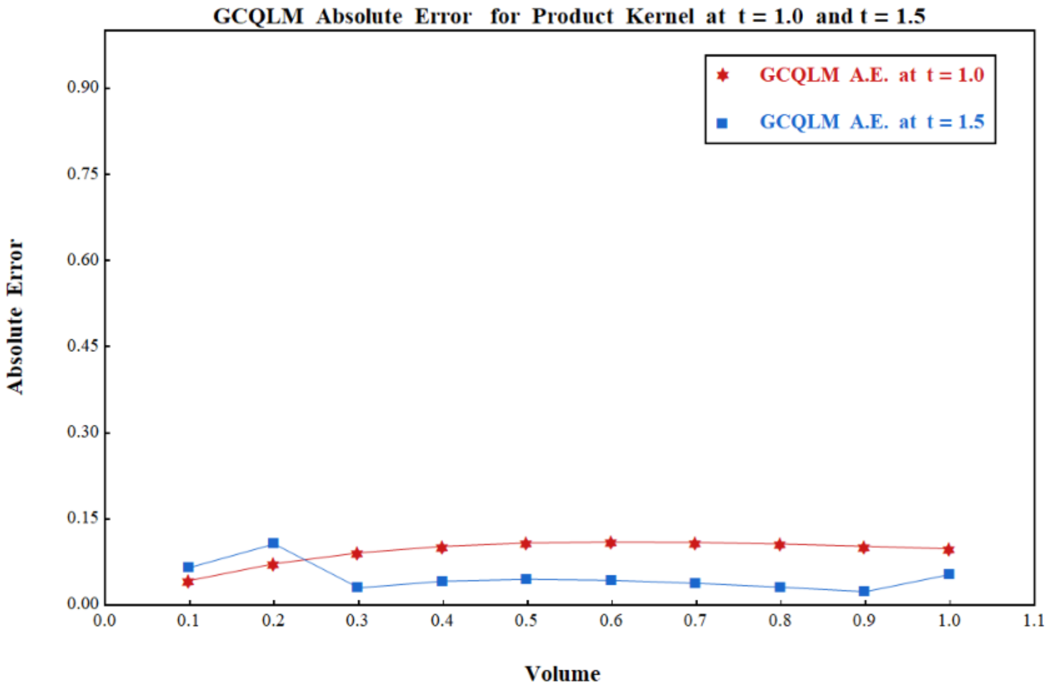


**Figure 6.** Graphical representation of the proposed GCQLM absolute error for the product kernel (Example 4.1) evaluated at $t = 1.0$ and $t = 1.5$.

The proposed framework effectively reduces error growth over time, showcasing strong error-decay characteristics. Its computational efficiency is obvious with a total CPU execution time of 59.83 seconds at $t = 1.0$ and an average step duration of 0.60 seconds at $t = 1.5$ (Table 6). These results establish the GCQLM as a reliable tool for dealing with nonlinear and stiff aggregation profiles, offering better spatial precision and faster convergence than traditional semi-analytical methods.

**Table 6.** Computational efficiency metrics for the GCQLM solver using the product kernel ($t = 1.5$).

| Performance Metric | GCQLM CPU Time |
|---|---|
| Total Computational CPU Time | 94.3350 seconds |
| Average CPU Time Per Step | 0.628900 seconds |

**Example 4.2. Constant kernel $l(p, q) = 1$ with an initial exponential volume distribution $u_0(p) = e^{-p}$.**

Consider the continuous CPBM governed by the constant aggregation kernel $l(p, q) = 1$ with an initial exponential volume distribution $u_0(p) = e^{-p}$. Under this kinetic condition, the transport equation reduces to the nonlinear integro-differential equation,

$$\frac{\partial u(p,t)}{\partial t} = \frac{1}{2}\int_0^p u(p-q,t)u(q,t)\,dq - u(p,t)\int_0^\infty u(q,t)\,dq, \quad p \in [0,\infty), \quad t \in [0,T]. \tag{4.6}$$

The analytical exact solution for this standard aggregation process is,

$$u(p,t) = \frac{4\exp\left(\frac{-2p}{2+t}\right)}{(2+t)^2}. \tag{4.7}$$

Define the zeroth moment (total particle number) as

$$M_0(t) = \int_0^\infty u(q,t)\,dq,$$

which tracks the dynamic total number of particles.

The nonlinear aggregation operator $\mathcal{F}(u)$ is defined by

$$\mathcal{F}(u)(p) = \frac{1}{2}\int_0^p u(p-q,t)u(q,t)\,dq - u(p,t)M_0(t). \tag{4.8}$$

Let $u^{(n)}(p,t)$ denote the solution at current quasilinearization iteration step $n$, and $h(p,t) = u^{(n+1)}(p,t) - u^{(n)}(p,t)$ be an arbitrary small perturbation.

The linear Fréchet derivative $\mathcal{F}'(u^{(n)})[h]$ is given by the directional Gâteaux derivative limit,

$$\mathcal{F}'(u^{(n)})[h](p) = \lim_{\epsilon\to 0}\frac{\mathcal{F}(u^{(n)}+\epsilon h)(p) - \mathcal{F}(u^{(n)})(p)}{\epsilon}.$$

Expanding the source integral term under perturbation gives,

$$\begin{aligned}\mathcal{R}_{\mathrm{f}}(u^{(n)}+\epsilon h)(p) &= \frac{1}{2}\int_0^p \left[u^{(n)}(p-q)+\epsilon h(p-q)\right]\left[u^{(n)}(q)+\epsilon h(q)\right]\,dq\\ &= \frac{1}{2}\int_0^p u^{(n)}(p-q)u^{(n)}(q)\,dq + \frac{\epsilon}{2}\int_0^p \left[h(p-q)u^{(n)}(q)+u^{(n)}(p-q)h(q)\right]dq + O(\epsilon^2).\end{aligned}$$

Similarly, expanding the sink term gives,

$$\begin{aligned}\mathcal{R}_{\mathrm{s}}(u^{(n)}+\epsilon h)(p) &= \left[u^{(n)}(p)+\epsilon h(p)\right]\int_0^\infty \left[u^{(n)}(q)+\epsilon h(q)\right]dq\\ &= u^{(n)}(p)M^{(n)} + \epsilon h(p)M^{(n)} + \epsilon u^{(n)}(p)H + O(\epsilon^2),\end{aligned}$$

where

$$M^{(n)} = \int_0^\infty u^{(n)}(q)dq, \quad H = \int_0^\infty h(q)dq.$$

Subtracting the unmodified operator and taking the limit gives the exact linear Fréchet derivative,

$$\mathcal{F}'(u^{(n)})[h](p) = \frac{1}{2}\int_0^p \left[h(p-q)u^{(n)}(q)+u^{(n)}(p-q)h(q)\right]dq - h(p)M^{(n)} - u^{(n)}(p)H. \tag{4.9}$$

The quasilinearization iterative update is governed by,

$$\frac{\partial u^{(n+1)}(p,t)}{\partial t} - \mathcal{F}'(u^{(n)})[u^{(n+1)}](p,t) = \mathcal{F}(u^{(n)})(p,t) - \mathcal{F}'(u^{(n)})[u^{(n)}](p,t).$$

Substituting explicit operators in the above gives the linearized PDE,

$$\begin{aligned}\frac{\partial u^{(n+1)}(p,t)}{\partial t} &= \frac{1}{2}\int_0^p u^{(n+1)}(p-q,t)u^{(n)}(q,t)dq + \frac{1}{2}\int_0^p u^{(n)}(p-q,t)u^{(n+1)}(q,t)dq \\ &- M^{(n)}u^{(n+1)}(p,t) - u^{(n)}(p,t)M^{(n+1)}(t) \\ &- \frac{1}{2}\int_0^p u^{(n)}(p-q,t)u^{(n)}(q,t)dq + u^{(n)}(p,t)M^{(n)}(t),\end{aligned} \tag{4.10}$$

where

$$M^{(n+1)}(t) = \int_0^\infty u^{(n+1)}(q,t)dq.$$

Following the approach detailed in Example 4.1, the continuous linearized system (4.10) is discretized on Chebyshev–Gauss–Lobatto nodes with domain truncation $[0, P_{\max}]$, coordinate mapping, and Clenshaw–Curtis quadrature.

The discrete Jacobian matrix $A^{(n)} \in \mathbb{R}^{(N+1)\times(N+1)}$ entries are assembled as,

$$A_{ij}^{(n)} = \frac{P_{\max}}{4}\left[u_j^{(n)}(I_{i,j})_j + u^{(n)}(p_i - p_j)\delta_{ij}\right]w_j - M^{(n)}\delta_{ij} - \frac{P_{\max}}{2}u_i^{(n)}w_j,$$

where $M^{(n)}$ is the zeroth moment of $u^{(n)}$.

The forcing vector $S^{(n)}$ is evaluated as,

$$S_i^{(n)} = -\frac{P_{\max}}{4}\sum_{k=0}^{N}\mathcal{I}[u^{(n)}](p_i - p_k)u_k^{(n)}w_k + M^{(n)}u_i^{(n)}.$$

Implicit backward Euler time discretization and iterative solver procedures follow as in Example 4.1.

For Example 4.2, the graphical comparisons of the GCQLM solution against the VIM, HAM, MVIM, and the exact analytical solution for the constant aggregation kernel $\ell(p,q) = 1$ under an exponential initial condition $u_0(p) = e^{-p}$ are illustrated in Figures 7 and 8. The GCQLM demonstrates exceptional agreement with the exact analytical solution at both short-term ($t = 0.85$) and long-term ($t = 4.0$) conditions. Conversely, traditional methods such as the VIM, HAM, and MVIM exhibit significant tracking deviations, as quantitatively detailed in Table 7. The computational execution profiles under short-term conditions are captured in Table 8. Subsequently, the data comparisons and structural convergence limits at the long-time limit are detailed in Table 9.

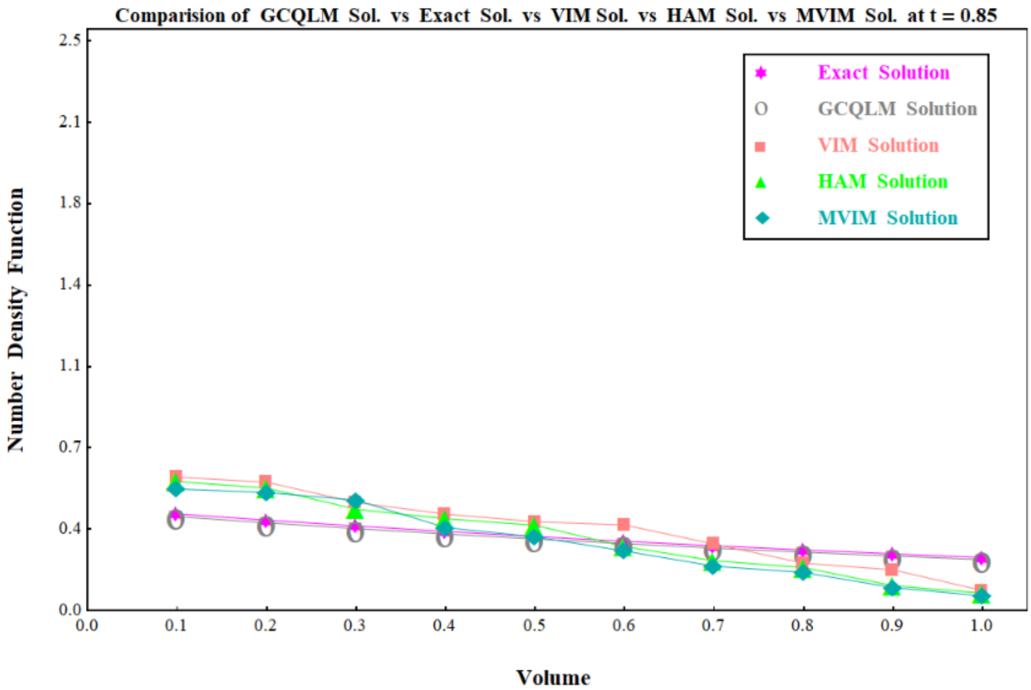


**Figure 7.** Comparison of the proposed GCQLM solution against the exact, VIM, HAM, and MVIM solutions for the constant kernel (Example 4.2) at time $t = 0.85$.

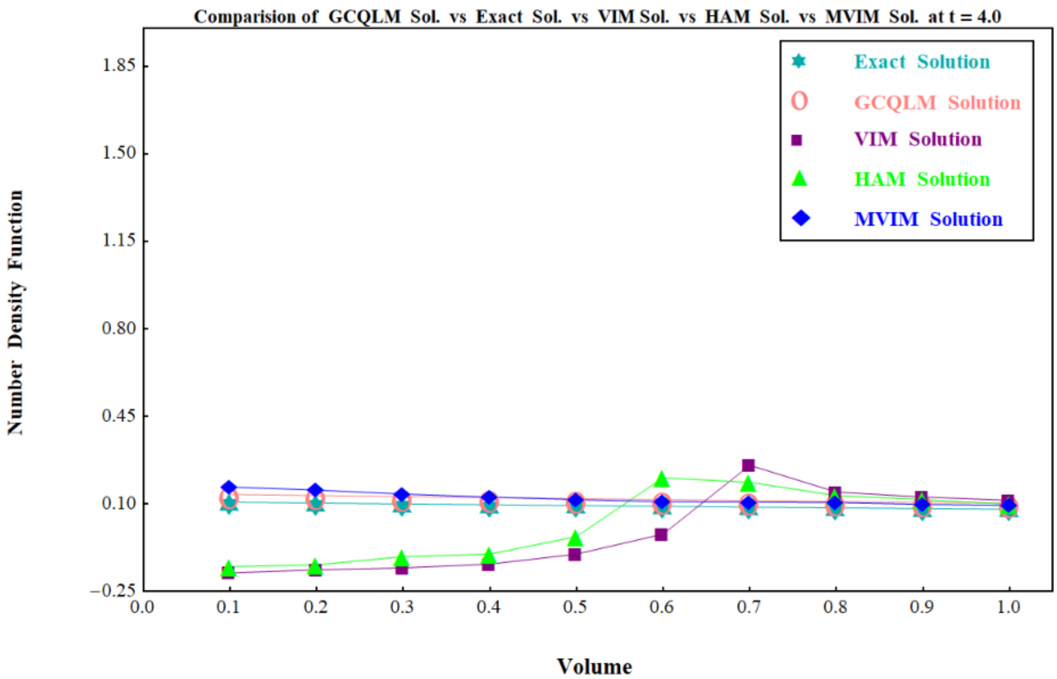


**Figure 8.** Comparison of the proposed GCQLM solution against the exact, VIM, HAM, and MVIM solutions for the constant kernel (Example 4.2) at time $t = 4.0$.

**Table 7.** Numerical comparison and verification for the CPBM with exact, absolute error, VIM, HAM, and MVIM solutions for the constant kernel ($t = 0.85$) using the MATHEMATICA WOLFRAM 9 software.

| Volume $(p)$ | GCQLM | Exact Solution | GCQLM A.E. | VIM | HAM | MVIM |
|---|---|---|---|---|---|---|
| 0.1 | 0.40427052 | 0.41578088 | 0.0115 | 0.574 | 0.555 | 0.523 |
| 0.2 | 0.37765059 | 0.38896592 | 0.0113 | 0.552 | 0.527 | 0.508 |
| 0.3 | 0.35280012 | 0.36388033 | 0.0111 | 0.465 | 0.436 | 0.475 |
| 0.4 | 0.32958830 | 0.34041259 | 0.0108 | 0.415 | 0.395 | 0.357 |
| 0.5 | 0.30790680 | 0.31845836 | 0.0106 | 0.382 | 0.367 | 0.317 |
| 0.6 | 0.28765448 | 0.29792002 | 0.0103 | 0.368 | 0.275 | 0.256 |
| 0.7 | 0.26873718 | 0.27870626 | 0.0100 | 0.286 | 0.214 | 0.191 |
| 0.8 | 0.25106584 | 0.26073165 | 0.0097 | 0.204 | 0.185 | 0.164 |
| 0.9 | 0.23455935 | 0.24391628 | 0.0094 | 0.175 | 0.107 | 0.099 |
| 1.0 | 0.21913951 | 0.22818539 | 0.0090 | 0.086 | 0.075 | 0.063 |

**Table 8.** Computational efficiency metrics for the GCQLM solver using the constant kernel ($t = 0.85$).

| Performance Metric | GCQLM CPU Time |
|---|---|
| Total Computational CPU Time | 44.9838 seconds |
| Average CPU Time Per Step | 0.529222 seconds |

**Table 9.** Numerical comparison and verification for the CPBM with exact, absolute error, VIM, HAM, and MVIM solutions for the constant kernel ($t = 4$) using the MATHEMATICA WOLFRAM 9 software.

| Volume $(p)$ | GCQLM | Exact Solution | GCQLM A.E. | VIM | HAM | MVIM |
|---|---|---|---|---|---|---|
| 0.1 | 0.13841281 | 0.10746846 | 0.0309 | −0.175 | −0.150 | 0.168 |
| 0.2 | 0.13401830 | 0.10394522 | 0.0301 | −0.163 | −0.143 | 0.156 |
| 0.3 | 0.12977154 | 0.10053749 | 0.0292 | −0.155 | −0.110 | 0.140 |
| 0.4 | 0.12566108 | 0.09724148 | 0.0284 | −0.140 | −0.100 | 0.128 |
| 0.5 | 0.12168243 | 0.09405352 | 0.0276 | −0.100 | −0.030 | 0.118 |
| 0.6 | 0.11783125 | 0.09097008 | 0.0269 | −0.020 | 0.205 | 0.109 |
| 0.7 | 0.11410357 | 0.08798773 | 0.0261 | 0.255 | 0.187 | 0.108 |
| 0.8 | 0.11049468 | 0.08510315 | 0.0254 | 0.148 | 0.134 | 0.106 |
| 0.9 | 0.10700158 | 0.08231314 | 0.0247 | 0.128 | 0.118 | 0.099 |
| 1.0 | 0.10361956 | 0.07961459 | 0.0240 | 0.115 | 0.099 | 0.095 |

The tabular results further highlight that the GCQLM minimizes the absolute error norms to ultra-low values of 0.0090 at $t = 0.85$ and 0.024 at $t = 4.0$. As plotted in Figure 9, the proposed framework effectively stabilizes the residuals across various time levels. The computational efficiency of this approach is also reflected in the modest total CPU execution time of 44.98 seconds at $t = 0.85$ (Table 8) and a total CPU time of 221.19 seconds at the long-time limit $t = 4.0$ (Table 10). In summary, the GCQLM demonstrates superior accuracy and robust asymptotic numerical stability compared to traditional expansion methodologies, establishing its capability to efficiently handle highly nonlinear integro-differential systems under constant kinetic conditions.

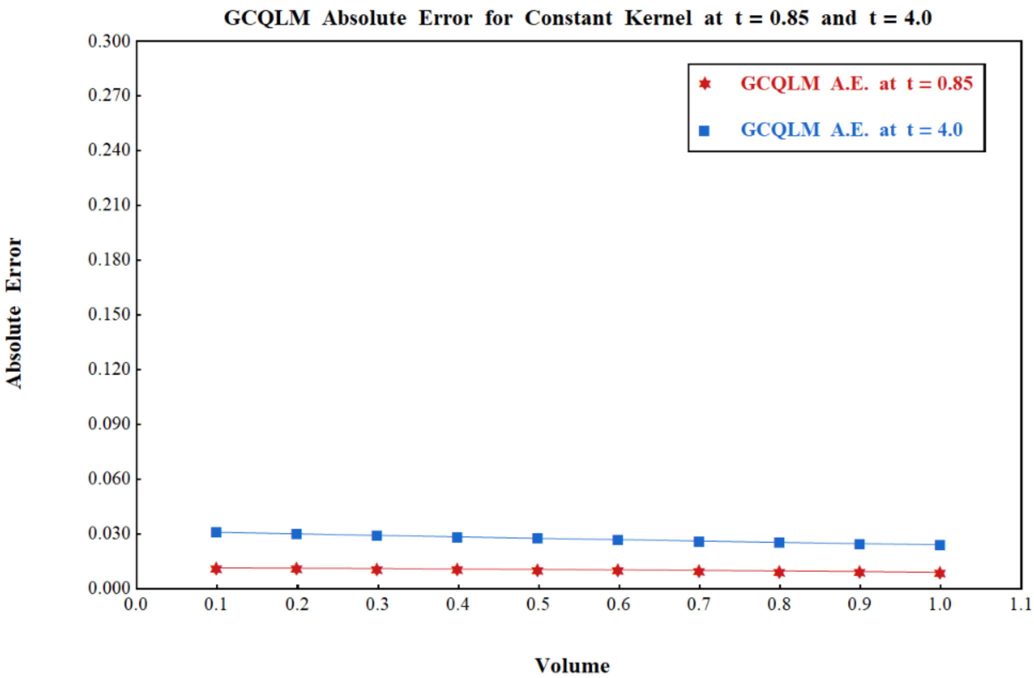


**Figure 9.** Graphical representation of the proposed GCQLM absolute error for the constant kernel (Example 4.2) evaluated at $t = 0.85$ and $t = 4.0$.

**Table 10.** Computational efficiency metrics for the GCQLM solver using the constant kernel ($t = 4$).

| Performance Metric | GCQLM CPU Time |
|---|---|
| Total Computational CPU Time | 221.1900 seconds |
| Average CPU Time Per Step | 0.552975 seconds |

**Example 4.3. Sum kernel $l(p, q) = p + q$ with an initial exponential distribution $u_0(p) = e^{-p}$.**

Consider the continuous CPBM governed by the sum aggregation kernel $l(p, q) = p + q$ with an initial exponential distribution $u_0(p) = e^{-p}$. By substituting the kernel into birth convolution operator, the relation simplifies to $l(p - q, q) = (p - q) + q = p$. Thus, the continuous non-linear transport equation reduces to,

$$\frac{\partial u(p,t)}{\partial t} = \frac{1}{2}\int_0^p p\, u(p-q,t)u(q,t)\,dq - u(p,t)\int_0^\infty (p+q)u(q,t)\,dq, \quad p \in [0,\infty), \quad t \in [0,T]. \tag{4.11}$$

Using the dynamic zeroth and first moments,

$$M_0(t) = \int_0^\infty u(q,t)\,dq, \quad M_1(t) = \int_0^\infty q u(q,t)\,dq,$$

the transport equation is expressed as,

$$\frac{\partial u(p,t)}{\partial t} = \frac{1}{2}\int_0^p p\, u(p-q,t)u(q,t)\, dq - u(p,t)\left[pM_0(t) + M_1(t)\right]. \tag{4.12}$$

The exact solution for this sum kernel aggregation process involves the modified Bessel function of the first kind $I_1(x)$ and is given by,

$$u(p,t) = \frac{(1-\sigma(t))e^{-(1+\sigma(t))p}}{p\sqrt{\sigma(t)}} I_1\left(2p\sqrt{\sigma(t)}\right), \tag{4.13}$$

where $\sigma(t) = 1 - e^{-t}$.

Defining the nonlinear aggregation operator $\mathcal{F}(u)$ for this system,

$$\mathcal{F}(u)(p) = \frac{1}{2}\int_0^p p\, u(p-q,t)u(q,t)\, dq - u(p,t)\left[p\int_0^\infty u(q,t)\, dq + \int_0^\infty qu(q,t)\, dq\right]. \tag{4.14}$$

Let $u^{(n)}(p,t)$ be the solution profile at iteration $n$, and $h(p,t) = u^{(n+1)}(p,t) - u^{(n)}(p,t)$ a small perturbation. The Fréchet derivative $\mathcal{F}'(u^{(n)})[h]$ is the directional Gâteaux derivative,

$$\mathcal{F}'(u^{(n)})[h](p) = \lim_{\epsilon\to 0}\frac{\mathcal{F}(u^{(n)} + \epsilon h)(p) - \mathcal{F}(u^{(n)})(p)}{\epsilon}.$$

Expanding the modified source term,

$$\begin{aligned}
\mathcal{R}_{\mathrm{f}}(u^{(n)} + \epsilon h)(p) &= \frac{1}{2}\int_0^p p\left[u^{(n)}(p-q) + \epsilon h(p-q)\right]\left[u^{(n)}(q) + \epsilon h(q)\right] dq \\
&= \frac{1}{2}\int_0^p p\, u^{(n)}(p-q)u^{(n)}(q)dq + \frac{\epsilon}{2}\int_0^p p\left[h(p-q)u^{(n)}(q) + u^{(n)}(p-q)h(q)\right] dq + O(\epsilon^2).
\end{aligned}$$

Similarly, expanding the modified sink term,

$$\begin{aligned}
\mathcal{R}_{\mathrm{s}}(u^{(n)} + \epsilon h)(p) &= \left[u^{(n)}(p) + \epsilon h(p)\right]\left[p\int_0^\infty \left(u^{(n)}(q) + \epsilon h(q)\right) dq + \int_0^\infty q\left(u^{(n)}(q) + \epsilon h(q)\right) dq\right] \\
&= u^{(n)}(p)\left[pM_0^{(n)} + M_1^{(n)}\right] + \epsilon h(p)\left[pM_0^{(n)} + M_1^{(n)}\right] \\
&\quad + \epsilon u^{(n)}(p)\left[p\int_0^\infty h(q)dq + \int_0^\infty qh(q)dq\right] + O(\epsilon^2).
\end{aligned}$$

Subtracting the unmodified operator, dividing by $\epsilon$, and taking the limit generates exact linear Fréchet derivative,

$$\begin{aligned}
\mathcal{F}'(u^{(n)})[h](p) = \frac{1}{2}\int_0^p p\left[h(p-q)u^{(n)}(q) + u^{(n)}(p-q)h(q)\right] dq \\
- h(p)\left[pM_0^{(n)} + M_1^{(n)}\right] - u^{(n)}(p)\left[pM_0(h) + M_1(h)\right],
\end{aligned} \tag{4.15}$$

where $M_k^{(n)} = \int_0^\infty q^k u^{(n)}(q)dq$ and $M_k(h) = \int_0^\infty q^k h(q)dq$ are moments evaluated at iteration $n$ and perturbation $h$, respectively.

The iterative linear update satisfies,

$$\frac{\partial u^{(n+1)}(p,t)}{\partial t} - \mathcal{F}'(u^{(n)})[u^{(n+1)}](p,t) = \mathcal{F}(u^{(n)})(p,t) - \mathcal{F}'(u^{(n)})[u^{(n)}](p,t).$$

Substituting and simplifying gives the linearized PIDE,

$$\begin{aligned}\frac{\partial u^{(n+1)}(p,t)}{\partial t} &= \frac{1}{2}\int_0^p p\left[u^{(n+1)}(p-q,t)u^{(n)}(q,t) + u^{(n)}(p-q,t)u^{(n+1)}(q,t)\right]dq \\ &\quad - u^{(n+1)}(p)\left[pM_0^{(n)} + M_1^{(n)}\right] - u^{(n)}(p)\left[pM_0^{(n+1)} + M_1^{(n+1)}\right] \\ &\quad - \frac{1}{2}\int_0^p p\,u^{(n)}(p-q,t)u^{(n)}(q,t)dq + u^{(n)}(p)\left[pM_0^{(n)} + M_1^{(n)}\right].\end{aligned} \tag{4.16}$$

The continuous system (4.21) involving the Pulvermacher kernel $l(p,q) = p^{2/3} + q^{2/3}$ is discretized on Chebyshev–Gauss–Lobatto nodes using the standard domain truncation $[0, P_{\max}]$, coordinate mapping, and Clenshaw–Curtis quadrature.

The discrete Jacobian matrix $A^{(n)} \in \mathbb{R}^{(N+1)\times(N+1)}$ has entries,

$$\begin{aligned}A_{ij}^{(n)} &= \frac{P_{\max}}{4}\left[\left((p_i - p_j)^{2/3} + p_j^{2/3}\right)u_j^{(n)}(I_{i,j})_j + \left((p_i - p_j)^{2/3} + p_j^{2/3}\right)u^{(n)}(p_i - p_j)\delta_{ij}\right]w_j \\ &\quad - \left(p_i^{2/3}M_0^{(n)} + M_{2/3}^{(n)}\right)\delta_{ij} - \frac{P_{\max}}{2}u_i^{(n)}(p_i^{2/3} + p_j^{2/3})w_j,\end{aligned}$$

where $M_0^{(n)}$ and $M_{2/3}^{(n)}$ denote the zeroth and fractional moments at iteration $n$.

The forcing vector is,

$$S_i^{(n)} = -\frac{P_{\max}}{4}\sum_{k=0}^{N}\left[(p_i - p_k)^{2/3} + p_k^{2/3}\right]\mathcal{I}[u^{(n)}](p_i - p_k)u_k^{(n)}w_k + \left(p_i^{2/3}M_0^{(n)} + M_{2/3}^{(n)}\right)u_i^{(n)}.$$

The implicit backward Euler time discretization and iterative resolution proceed as in previous examples.

The comparison of the Example 4.3 GCQLM solution against the VIM, OVIM, MVIM, and the exact analytical solution involving the modified Bessel function of the first kind, for the sum aggregation kernel $\ell(p,q) = p + q$ under an exponential initial distribution $u_0(p) = e^{-p}$, is illustrated in Figure 10. As tabulated in Table 11, the absolute error norm is recorded as 0.08. At the evaluated time level $t = 2.0$, the GCQLM performs exceptionally well and demonstrates close agreement with the exact benchmark solution, whereas the VIM, OVIM, and MVIM exhibit larger tracking deviations.

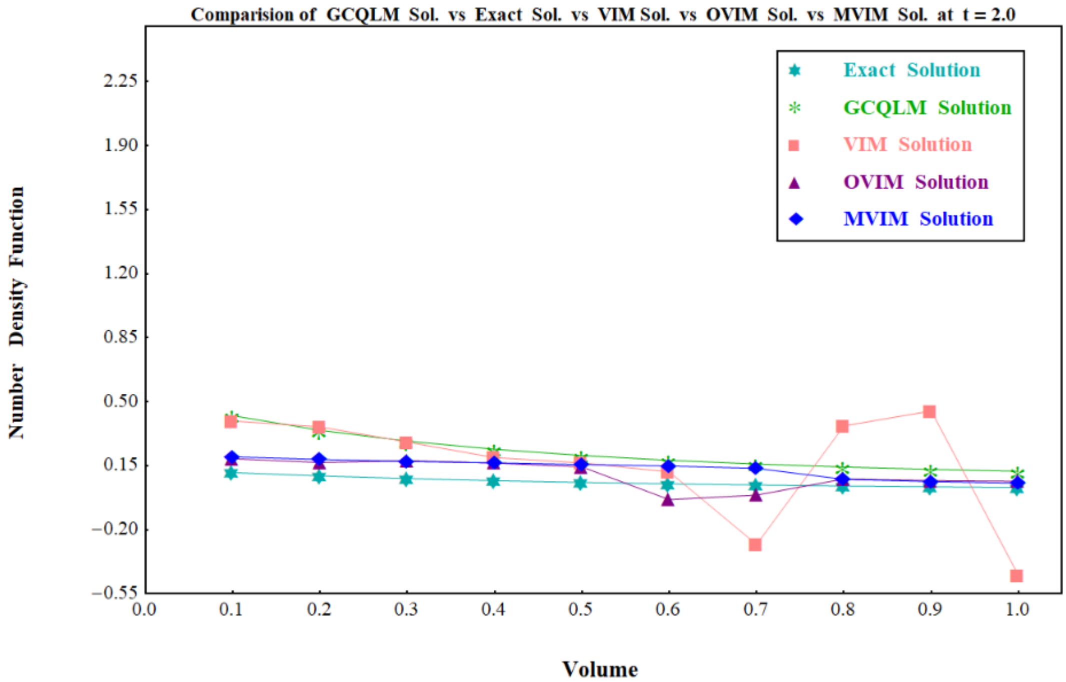


**Figure 10.** Comparison of the proposed GCQLM solution against the exact, VIM, OVIM, and MVIM solutions for the sum kernel (Example 4.3) at time $t = 2.0$.

**Table 11.** Numerical comparison and verification for the CPBM with exact, absolute error, VIM, OVIM, and MVIM solutions for the sum kernel ($t = 2$) using the MATHEMATICA WOLFRAM 9 software.

| Volume ($p$) | GCQLM | Exact Solution | GCQLM A.E. | VIM | OVIM | MVIM |
|---|---|---|---|---|---|---|
| 0.1 | 0.42421711 | 0.11279917 | 0.3114 | 0.395 | 0.189 | 0.199 |
| 0.2 | 0.34411284 | 0.09482813 | 0.2493 | 0.363 | 0.168 | 0.185 |
| 0.3 | 0.28485600 | 0.08040020 | 0.2045 | 0.280 | 0.178 | 0.174 |
| 0.4 | 0.24037456 | 0.06873668 | 0.1716 | 0.195 | 0.165 | 0.166 |
| 0.5 | 0.20650501 | 0.05924173 | 0.1473 | 0.166 | 0.144 | 0.157 |
| 0.6 | 0.18035386 | 0.05145749 | 0.1289 | 0.117 | −0.035 | 0.149 |
| 0.7 | 0.15988961 | 0.04503052 | 0.1149 | −0.280 | −0.010 | 0.136 |
| 0.8 | 0.14367078 | 0.03968673 | 0.1040 | 0.368 | 0.078 | 0.076 |
| 0.9 | 0.13066404 | 0.03521256 | 0.0955 | 0.450 | 0.069 | 0.0638 |
| 1.0 | 0.12011749 | 0.03144078 | 0.0887 | −0.450 | 0.065 | 0.055 |

Furthermore, the spatial absolute error norm decreases smoothly across the coordinate domain and reaches minimal, bounded values, as shown in the error profile plotted in Figure 11. The computational efficiency of this spectral-based quasilinearization approach is highlighted by a total CPU execution time of 118.74 seconds at $t = 2.0$, corresponding to a modest average duration of approximately 0.59 seconds per time step (Table 12). These metrics clearly validate that the GCQLM provides a significant structural advantage over standard analytical expansion procedures, ensuring rapid quadratic convergence coupled with outstanding reliability when capturing mass distribution trajectories.

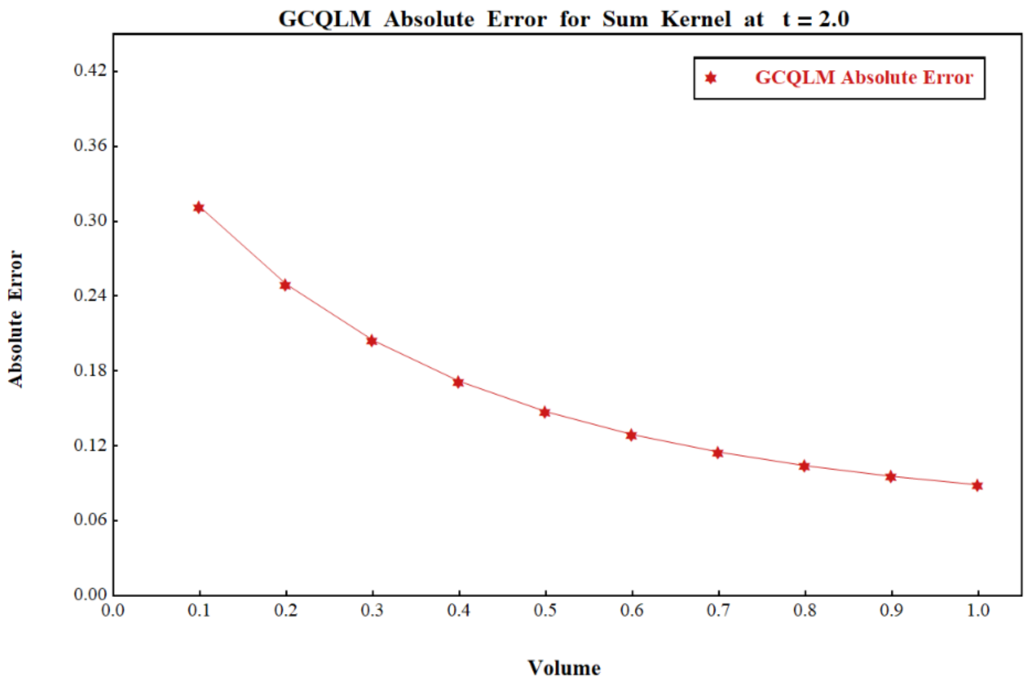


**Figure 11.** Graphical representation of the proposed GCQLM absolute error for the sum kernel (Example 4.3) evaluated at $t = 2.0$.

**Table 12.** Computational efficiency metrics for the GCQLM solver using the sum kernel ($t = 2$).

| Performance Metric | GCQLM CPU Time |
|---|---|
| Total Computational CPU Time | 118.7404 seconds |
| Average CPU Time Per Step | 0.593702 seconds |

**Example 4.4. Pulvermacher Kernel $l(p, q) = p^{2/3} + q^{2/3}$ with an initial exponential distribution $u_0(p) = e^{-p}$.**

Consider the CPBM governed by the non-integer power Pulvermacher aggregation kernel $l(p, q) = p^{2/3} + q^{2/3}$ with an initial exponential distribution $u_0(p) = e^{-p}$. Under this complex kinetic scenario, the continuous transport equation is given by the nonlinear partial integro-differential equation,

$$\frac{\partial u(p,t)}{\partial t} = \frac{1}{2}\int_0^p \left[(p-q)^{2/3} + q^{2/3}\right] u(p-q,t)u(q,t)\,dq - u(p,t)\int_0^\infty \left(p^{2/3} + q^{2/3}\right) u(q,t)\,dq, \quad (4.17)$$

where the standard zeroth moment ( i.e., representing the total particle number density) is defined as

$$M_0(t) = \int_0^\infty u(q,t)\,dq,$$

alongside the fractional volume-order particle moment (which physically captures mass distribution adjustments across non-integer dimensions) as,

$$M_{2/3}(t) = \int_0^\infty q^{2/3} u(q,t)\, dq.$$

The continuous transport structure simplifies by using macro-scale distribution dependencies to ,

$$\frac{\partial u(p,t)}{\partial t} = \frac{1}{2}\int_0^p \left[(p-q)^{2/3} + q^{2/3}\right] u(p-q,t)u(q,t)\, dq - u(p,t)\left[p^{2/3}M_0(t) + M_{2/3}(t)\right]. \tag{4.18}$$

The nonlinear aggregation operator $\mathcal{F}(u)$ is,

$$\mathcal{F}(u)(p) = \frac{1}{2}\int_0^p \left[(p-q)^{2/3} + q^{2/3}\right] u(p-q,t)u(q,t)\, dq - u(p,t)\left[p^{2/3}M_0(t) + M_{2/3}(t)\right]. \tag{4.19}$$

Let $u^{(n)}(p,t)$ denote the current iterate solution, and $h(p,t) = u^{(n+1)}(p,t) - u^{(n)}(p,t)$ a small perturbation. The Fréchet derivative $\mathcal{F}'(u^{(n)})[h]$ is defined by the limit,

$$\mathcal{F}'(u^{(n)})[h](p) = \lim_{\epsilon\to 0} \frac{\mathcal{F}(u^{(n)} + \epsilon h)(p) - \mathcal{F}(u^{(n)})(p)}{\epsilon}.$$

Expanding the modified birth term,

$$\begin{aligned}
\mathcal{R}_{\mathrm{f}}(u^{(n)} + \epsilon h)(p) &= \frac{1}{2}\int_0^p \left[(p-q)^{2/3} + q^{2/3}\right]\left[u^{(n)}(p-q) + \epsilon h(p-q)\right]\left[u^{(n)}(q) + \epsilon h(q)\right] dq \\
&= \frac{1}{2}\int_0^p \left[(p-q)^{2/3} + q^{2/3}\right] u^{(n)}(p-q)u^{(n)}(q) dq \\
&\quad + \frac{\epsilon}{2}\int_0^p \left[(p-q)^{2/3} + q^{2/3}\right]\left[h(p-q)u^{(n)}(q) + u^{(n)}(p-q)h(q)\right] dq + O(\epsilon^2).
\end{aligned}$$

Expanding the modified sink term,

$$\begin{aligned}
\mathcal{R}_{\mathrm{s}}(u^{(n)} + \epsilon h)(p) &= \left[u^{(n)}(p) + \epsilon h(p)\right]\left[p^{2/3}\int_0^\infty \left(u^{(n)}(q) + \epsilon h(q)\right) dq + \int_0^\infty q^{2/3}\left(u^{(n)}(q) + \epsilon h(q)\right) dq\right] \\
&= u^{(n)}(p)\left[p^{2/3}M_0^{(n)} + M_{2/3}^{(n)}\right] + \epsilon h(p)\left[p^{2/3}M_0^{(n)} + M_{2/3}^{(n)}\right] \\
&\quad + \epsilon u^{(n)}(p)\left[p^{2/3}\int_0^\infty h(q)dq + \int_0^\infty q^{2/3}h(q)dq\right] + O(\epsilon^2).
\end{aligned}$$

Taking the difference, dividing by $\epsilon$, and taking the limit gives the Fréchet derivative,

$$\begin{aligned}
\mathcal{F}'(u^{(n)})[h](p) = \frac{1}{2}\int_0^p &\left[(p-q)^{2/3} + q^{2/3}\right]\left[h(p-q)u^{(n)}(q) + u^{(n)}(p-q)h(q)\right] dq \\
&- h(p)\left[p^{2/3}M_0^{(n)} + M_{2/3}^{(n)}\right] - u^{(n)}(p)\left[p^{2/3}M_0(h) + M_{2/3}(h)\right],
\end{aligned} \tag{4.20}$$

where $M_k^{(n)} = \int_0^\infty q^k u^{(n)}(q)dq$ and $M_k(h) = \int_0^\infty q^k h(q)dq$.

The iterative update satisfies,

$$\frac{\partial u^{(n+1)}(p,t)}{\partial t} - \mathcal{F}'(u^{(n)})[u^{(n+1)}](p,t) = \mathcal{F}(u^{(n)})(p,t) - \mathcal{F}'(u^{(n)})[u^{(n)}](p,t).$$

Substituting and grouping terms generates the linearized PIDE,

$$\begin{aligned}\frac{\partial u^{(n+1)}(p,t)}{\partial t} &= \frac{1}{2}\int_0^p \left[(p-q)^{2/3}+q^{2/3}\right]\left[u^{(n+1)}(p-q,t)u^{(n)}(q,t)+u^{(n)}(p-q,t)u^{(n+1)}(q,t)\right]dq \\ &- u^{(n+1)}(p)\left[p^{2/3}M_0^{(n)}+M_{2/3}^{(n)}\right]-u^{(n)}(p)\left[p^{2/3}M_0^{(n+1)}+M_{2/3}^{(n+1)}\right] \\ &- \frac{1}{2}\int_0^p \left[(p-q)^{2/3}+q^{2/3}\right]u^{(n)}(p-q,t)u^{(n)}(q,t)dq+u^{(n)}(p)\left[p^{2/3}M_0^{(n)}+M_{2/3}^{(n)}\right],\end{aligned} \tag{4.21}$$

where $M_k^{(n+1)} = \int_0^\infty q^k u^{(n+1)}(q)dq$.

The continuous system (4.21) involving the Pulvermacher kernel $l(p,q) = p^{2/3}+q^{2/3}$ is differentiated on Chebyshev–Gauss–Lobatto nodes using the standard domain truncation $[0, P_{\max}]$, coordinate mapping, and Clenshaw–Curtis quadrature.

The discrete Jacobian matrix $A^{(n)} \in \mathbb{R}^{(N+1)\times(N+1)}$ has entries,

$$\begin{aligned}A_{ij}^{(n)} &= \frac{P_{\max}}{4}\left[\left((p_i-p_j)^{2/3}+p_j^{2/3}\right)u_j^{(n)}(I_{i,j})_j+\left((p_i-p_j)^{2/3}+p_j^{2/3}\right)u^{(n)}(p_i-p_j)\delta_{ij}\right]w_j \\ &- \left(p_i^{2/3}M_0^{(n)}+M_{2/3}^{(n)}\right)\delta_{ij}-\frac{P_{\max}}{2}u_i^{(n)}(p_i^{2/3}+p_j^{2/3})w_j,\end{aligned}$$

where $M_0^{(n)}$ and $M_{2/3}^{(n)}$ denote the zeroth and fractional moments at iteration $n$.

The forcing vector is,

$$S_i^{(n)} = -\frac{P_{\max}}{4}\sum_{k=0}^{N}\left[(p_i-p_k)^{2/3}+p_k^{2/3}\right]\mathcal{I}[u^{(n)}](p_i-p_k)u_k^{(n)}w_k+\left(p_i^{2/3}M_0^{(n)}+M_{2/3}^{(n)}\right)u_i^{(n)}.$$

The implicit backward Euler time discretization and iterative resolution proceed as in previous examples.

Graphical comparisons in Figures 12 and 13 illustrate the performance of the GCQLM solution against the VIM, MVIM, and FVS solutions for the Pulvermacher kernel $\ell(p,q) = p^{2/3}+q^{2/3}$ under a standard exponential initial distribution $u_0(p) = e^{-p}$. At the evaluated final time level $t = 1.0$, the GCQLM demonstrates remarkable accuracy by closely observing the reference distribution's graphical profile. Conversely, traditional techniques such as the VIM and MVIM exhibit significant tracking deviations, which are primarily attributed to inherent structural approximation limitations.

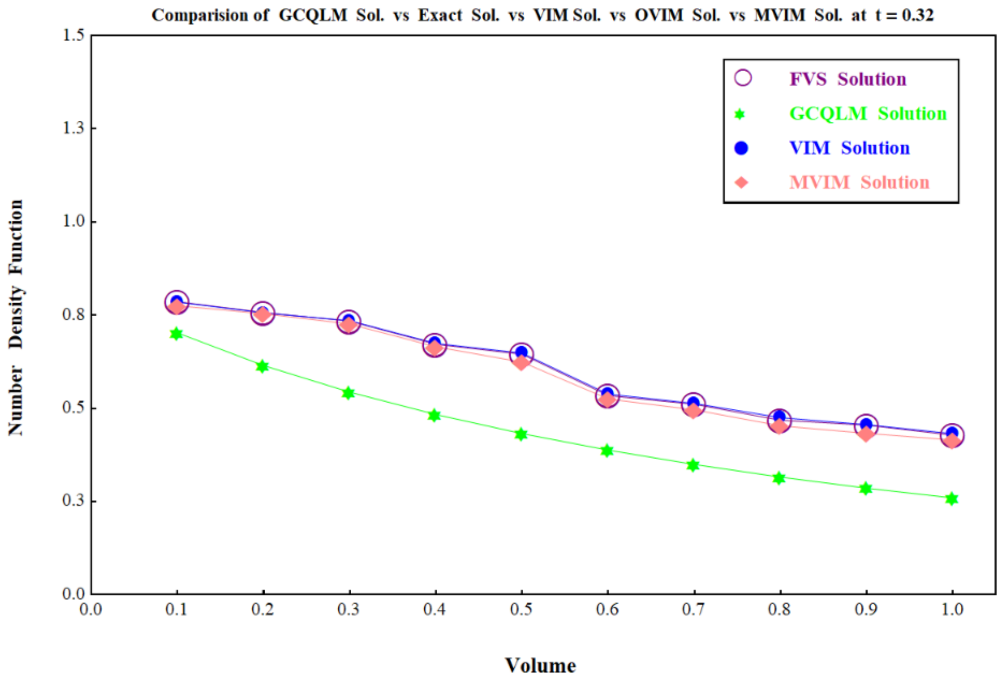


**Figure 12.** Comparison of the proposed GCQLM solution against the VIM, MVIM, and FVS reference solutions for the Pulvermacher kernel (Example 4.4) at time $t = 0.32$.

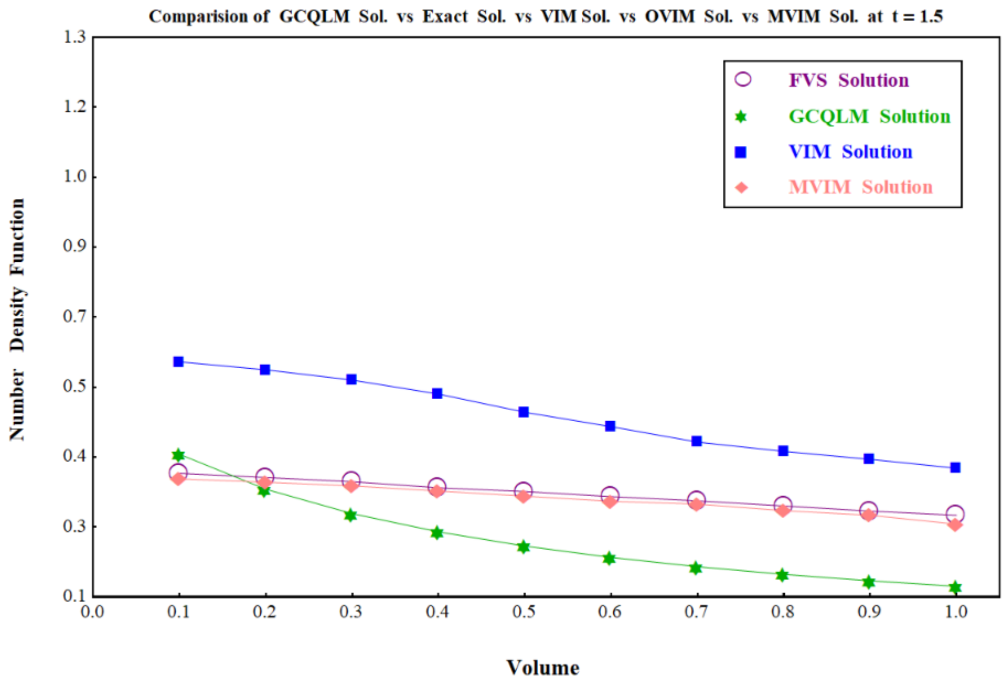


**Figure 13.** Comparison of the proposed GCQLM solution against the VIM, MVIM, and FVS reference solutions for the Pulvermacher kernel (Example 4.4) at time $t = 1.5$.

The corresponding absolute error norms decrease uniformly across the computational domain, resulting in minimal values of $2.63 \times 10^{-2}$ at $t = 0.32$ and $1.17 \times 10^{-2}$ at $t = 1.5$, as tabulated in

Table 13. As shown in Figure 14, the proposed framework maintains robust error reduction features, precisely mapping the spatial distribution and mass adjustments across fractional volume-order particle dimensions without generating arbitrary numerical oscillations. Furthermore, the solver remains highly computationally efficient; at $t = 0.32$, it requires a total CPU execution time of only 36.66 seconds, translating to an average step duration of approximately 1.15 seconds (Table 14). At the extended time level $t = 1.5$, the total and average CPU execution times are 156.76 seconds and 1.05 seconds, respectively. The GCQLM successfully addresses the non-integer kinetics of the Pulvermacher kernel, highlighting its robustness, fast convergence, and computational benefits compared to traditional analytical methods for stiff PBMs.

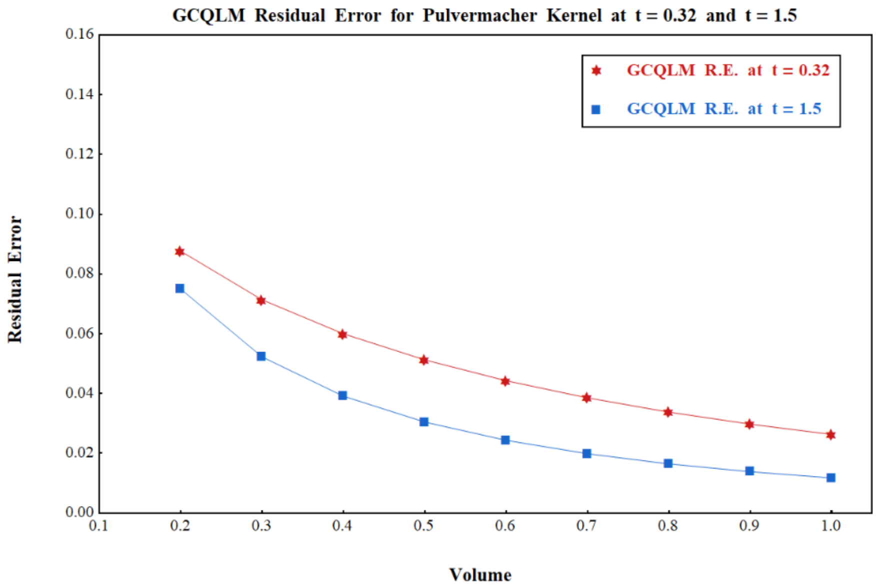


**Figure 14.** Graphical representation of the proposed GCQLM for the Pulvermacher kernel (Example 4.4) evaluated at $t = 0.32$ and $t = 1.5$.

**Table 13.** Numerical comparison and verification for the CPBM solution with residual error, VIM, MVIM, and FVS solutions for the Pulvermacher kernel ($t = 0.32$) using the MATHEMATICA WOLFRAM 9.

| Volume ($p$) | GCQLM | Residual Error | VIM | MVIM | FVS |
|---|---|---|---|---|---|
| 0.1 | 0.70240458 | — | 0.785 | 0.775 | 0.786 |
| 0.2 | 0.61476528 | $8.764 \times 10^{-2}$ | 0.756 | 0.754 | 0.757 |
| 0.3 | 0.54339266 | $7.137 \times 10^{-2}$ | 0.735 | 0.726 | 0.734 |
| 0.4 | 0.48339865 | $5.999 \times 10^{-2}$ | 0.674 | 0.665 | 0.672 |
| 0.5 | 0.43213539 | $5.126 \times 10^{-2}$ | 0.648 | 0.624 | 0.645 |
| 0.6 | 0.38785895 | $4.428 \times 10^{-2}$ | 0.538 | 0.525 | 0.534 |
| 0.7 | 0.34931287 | $3.855 \times 10^{-2}$ | 0.513 | 0.496 | 0.511 |
| 0.8 | 0.31554407 | $3.377 \times 10^{-2}$ | 0.475 | 0.453 | 0.468 |
| 0.9 | 0.28580659 | $2.974 \times 10^{-2}$ | 0.456 | 0.433 | 0.455 |
| 1.0 | 0.25950160 | $2.63 \times 10^{-2}$ | 0.432 | 0.415 | 0.428 |

**Table 14.** Computational efficiency metrics for the GCQLM solver using the Pulvermacher kernel ($t = 0.32$).

| Performance Metric | GCQLM CPU Time |
|---|---|
| Total Computational CPU Time | 36.6606 seconds |
| Average CPU Time Per Step | 1.145644 seconds |

### 4.1. *Quantitative error norm comparison and convergence rates*

To rigorously verify the accuracy and convergence of the GCQLM solver, we compute global error norms at the final time $t = 1.0$ for the product kernel example. The supremum norm ($L_\infty$) and root-mean-square norm ($L_2$) are computed as follows,

$$||e||_{L_\infty} = \max_{0\le i\le N} |u(p_i, t) - u_{\text{exact}}(p_i, t)|, \quad ||e||_{L_2} = \left( \frac{P_{\max}}{2} \sum_{j=0}^{N} |u(p_j, t) - u_{\text{exact}}(p_j, t)|^2 w_j \right)^{1/2},$$

where $N$ denotes the number of collocation points and $w_j$ are the Clenshaw–Curtis quadrature weights.

Table 1 presents the computed error norms and experimental convergence rates for the GCQLM, VIM, and MVIM as the number of collocation nodes $N$ increases. The GCQLM exhibits exceptional convergence characteristics, successfully achieving high-order spectral accuracy as theoretically proposed. Conversely, the VIM and MVIM exhibit nearly invariant error results across varying values of $N$, illustrating their limited spatial precision when handling higher-order representations.

These numerical findings align closely with the spatial convergence analysis detailed in Section 3.2 and illustrated in Figure 1, which plots the maximum absolute error ($L_\infty$ norm) of the GCQLM against $N$ on a log-linear scale. The exponential decay structure observed in that figure further validates the spectral convergence bounds established through the quantitative error metrics tabulated in Table 1.

In summary, the empirical evidence derived from the error norms and convergence trajectories clearly demonstrates the rapid iterative velocity and computational robustness of the GCQLM when simulating highly nonlinear CPBMs.

## 5. Conclusions

The proposed Global collocation quasi-linearization method (GCQLM) provides a highly effective and stable numerical framework for solving nonlinear CPBMs, demonstrating rapid iterative convergence throughout the entire process. By converting highly nonlinear aggregation operators into a sequence of linear spectral systems, the framework minimizes time-stepping errors and significantly enhances spatial resolution by using global orthogonal polynomial projections. The robustness of the GCQLM is verified through extensive numerical experiments conducted across four distinct benchmark aggregation profiles: the product, constant, sum, and Pulvermacher kernels. Comparative assessments demonstrate that the proposed scheme consistently outperforms existing semi-analytical and numerical methods, including the VIM, MVIM, HAM, OVIM, and the FVS. Rigorous error analyses detailed in Tables 3, 5, 7, 9, 11, 13, and 15, alongside graphical comparisons in Figures 4–14, confirm that the GCQLM achieves significantly smaller $L_\infty$ error norms, reaching an exceptional precision of $1.13 \times 10^{-12}$ for the product kernel configuration.

The algorithm demonstrates fast quadratic convergence in quasilinearization iterations (see Figure 3), achieving high spatial accuracy with exponential error decay as the number of collocation points increases (see Figure 1). It maintains first-order temporal accuracy using the implicit backward Euler scheme (see Figure 2). Graphical results show consistent error reduction, quick stabilization of residuals, and smooth mass profile reconstructions without artificial oscillations or non-physical boundary flows. Furthermore, the GCQLM reduces the absolute error norm for the product kernel to approximately 0.042 at $t = 1.0$ (Table 3), demonstrating excellent computational efficiency with a total CPU time of 59.83 seconds at $t = 1.0$ and a modest average step duration of 0.60 seconds at $t = 1.5$ (Table 6). For the constant kernel, the error norms remain bounded at 0.0090 for $t = 0.85$ and 0.024 for $t = 4.0$ (Tables 7 and 9), requiring total CPU execution times of 44.98 seconds and 221.19 seconds, respectively (Tables 8 and 10). Under the sum kernel, the spatial absolute error decreases smoothly to roughly 0.08 at $t = 2.0$ (Table 11), corresponding to a total CPU time of 118.74 seconds and an average of 0.59 seconds per time step (Table 12). Finally, for the more complex and highly nonlinear Pulvermacher kernel, the absolute errors decrease to $2.63 \times 10^{-2}$ at $t = 0.32$ and $1.17 \times 10^{-2}$ at $t = 1.5$ (Table 13). The computational performance is competitive, with total CPU times of 36.66 seconds at $t = 0.32$ and 156.76 seconds at $t = 1.5$, averaging about 1.15 seconds and 1.05 seconds per time step (Tables 14 and 16). This demonstrates the GCQLM's superiority in precision and computational efficiency across different kernel complexities.

**Table 15.** Numerical comparison and verification for the CPBM solution with residual error, VIM, MVIM, and FVS solutions for the Pulvermacher kernel ($t = 1.5$) using the MATHEMATICA WOLFRAM 9.

| Volume ($p$) | GCQLM | Residual Error | VIM | MVIM | FVS |
|---|---|---|---|---|---|
| 0.1 | 0.40571128 | — | 0.604 | 0.353 | 0.365 |
| 0.2 | 0.33077097 | $7.494 \times 10^{-2}$ | 0.587 | 0.346 | 0.356 |
| 0.3 | 0.27851889 | $5.225 \times 10^{-2}$ | 0.565 | 0.338 | 0.347 |
| 0.4 | 0.23940698 | $3.911 \times 10^{-2}$ | 0.535 | 0.327 | 0.334 |
| 0.5 | 0.20896530 | $3.044 \times 10^{-2}$ | 0.496 | 0.316 | 0.326 |
| 0.6 | 0.18461377 | $2.433 \times 10^{-2}$ | 0.465 | 0.305 | 0.315 |
| 0.7 | 0.16478458 | $1.985 \times 10^{-2}$ | 0.432 | 0.299 | 0.306 |
| 0.8 | 0.14833218 | $1.645 \times 10^{-2}$ | 0.412 | 0.285 | 0.295 |
| 0.9 | 0.13450878 | $1.382 \times 10^{-2}$ | 0.395 | 0.275 | 0.284 |
| 1.0 | 0.12275823 | $1.175 \times 10^{-2}$ | 0.376 | 0.256 | 0.275 |

**Table 16.** Computational efficiency metrics for the GCQLM solver using the Pulvermacher kernel ($t = 1.5$).

| Performance Metric | GCQLM CPU Time |
|---|---|
| Total Computational CPU Time | 156.7588 seconds |
| Average CPU Time Per Step | 1.045059 seconds |

In addition, the proposed method simplifies algorithm implementation by entirely eliminating the requirement for auxiliary convergence parameters while preserving strict numerical precision. It effectively handles highly nonlinear and stiff operators, making it an ideal choice for simulating complex particulate aggregations. By offering enhanced accuracy, ensured quadratic convergence, and reduced computational costs with respect to traditional algorithms, the GCQLM provides a robust framework for advanced population balance analysis. Future research directions will focus on extending this iterative spectral framework to weakly singular coalescence kernels and fractional-order operators, using recent advancements in fractional calculus and spectral methodologies to expand the general applicability of the GCQLM to singular PBMs.

## Author contributions

Taruni Alekhya Sarvasuddi: Conceptualization, data curation, formal analysis, investigation, methodology, project administration, software, resources, validation, visualization, writing – original draft, writing – review & editing; Prashanth Maroju: Conceptualization, formal analysis, funding acquisition, project administration, supervision, validation, visualization, review – editing; Sattam Alharbi: Formal analysis, funding acquisition, investigation, data curation, review – editing; Ramandeep Behl: Formal analysis, funding acquisition, investigation, data curation, review – editing. All authors have read and approved the final version of the manuscript for publication.

## Use of Generative-AI tools declaration

The authors declare that generative Artificial Intelligence (AI) tools were used solely to improve the language and clarity of the manuscript. No AI tools were used for core content generation, algorithmic layout, mathematical derivations, or data interpretation. All scientific work, calculations, tables, and analytical findings were created, reviewed, and validated exclusively by the authors.

## Acknowledgments

The authors extend their appreciation to Prince Sattam bin Abdulaziz University for funding this research work through the project number (PSAU/2026/01/41599).

## Funding statement

This study is supported via funding from Prince Sattam bin Abdulaziz University project number (PSAU/2026/01/41599).

## Conflict of interest

There is no conflict of interest.

## References

1. S. Yadav, M. Singh, S. Singh, S. Heinrich, J. Kumar, Modified variational iteration method and its convergence analysis for solving nonlinear aggregation population balance equation, *Comput. Fluids*, **274** (2024), 106233. https://doi.org/10.1016/j.compfluid.2024.106233

2. M. Singh, T. Matsoukas, G. Walker, Mathematical analysis of finite volume preserving scheme for nonlinear Smoluchowski equation, *Physica D*, **402** (2020), 132221. https://doi.org/10.1016/j.physd.2019.132221
3. M. Singh, H. Y. Ismail, T. Matsoukas, A. B. Albadarin, G. Walker, Mass-based finite volume scheme for aggregation, growth and nucleation population balance equation, *Proc. R. Soc. A*, **475** (2019), 20190552. http://dx.doi.org/10.1098/rspa.2019.0552
4. G. Kaur, R. Singh, H. Briesen, Approximate solutions of aggregation and breakage population balance equations, *J. Math. Anal. Appl.*, **512** (2022), 126166. https://doi.org/10.1016/j.jmaa.2022.126166
5. A. Dutta, Z. Pınar, D. Constales, T. Öziş, Population balances involving aggregation and breakage through homotopy approaches, *Int. J. Chem. React. Eng.*, **16** (2018), 20170153. https://doi.org/10.1515/ijcre-2017-0153
6. Z. Pınar, A. Dutta, G. Bény, T. Öziş, Analytical solution of population balance equation involving aggregation and breakage in terms of auxiliary equation method, *Pramana*, **84** (2015), 9–21. https://doi.org/10.1007/s12043-014-0838-y
7. D. Ramkrishna, *Population balances: Theory and applications to particulate systems in engineering*, Academic Press, 2000. https://doi.org/10.1016/B978-0-12-576970-9.X5000-0
8. D. L. Marchisio, R. O. Fox, Solution of population balance equations using the direct quadrature method of moments, *J. Aerosol Sci.*, **36** (2005), 43–73. https://doi.org/10.1016/j.jaerosci.2004.07.009
9. M. Kostoglou, A. J. Karabelas, A study of the nonlinear breakage equation: Analytical and asymptotic solutions, *J. Phys. A Math. Gen.*, **33** (2000), 1221–1232. https://doi.org/10.1088/0305-4470/33/6/309
10. M. Kostoglou, A. G. Konstandopoulos, S. K. Friedlander, Bivariate population dynamics simulation of fractal aerosol aggregate coagulation and restructuring, *J. Aerosol Sci.*, **37** (2006), 1102–1115. https://doi.org/10.1016/j.jaerosci.2005.11.009
11. M. Kostoglou, A. G. Konstandopoulos, Evolution of aggregate size and fractal dimension during Brownian coagulation, *J. Aerosol Sci.*, **32** (2001), 1399–1420. https://doi.org/10.1016/S0021-8502(01)00056-8
12. M. Kostoglou, S. Dovas, A. J. Karabelas, On the steady-state size distribution of dispersions in breakage processes, *Chem. Eng. Sci.*, **52** (1997), 1285–1299. https://doi.org/10.1016/S0009-2509(96)00488-5
13. S. Qamar, G. Warnecke, M. P. Elsner, On the solution of population balances for nucleation, growth, aggregation and breakage processes, *Chem. Eng. Sci.*, **64** (2009), 2088–2095. https://doi.org/10.1016/j.ces.2009.01.040
14. R. E. Bellman, R. E. Kalaba, *Quasilinearization and nonlinear boundary-value problems*, RAND Corporation, 1965.
15. N. H. Sweilam, M. M. Khader, A Chebyshev pseudo-spectral method for solving fractional-order integro-differential equations, *ANZIAM J.*, **51** (2010), 464–475. https://doi.org/10.1017/S1446181110000830

16. T. A. Sarvasuddi, P. Maroju, A global collocation quasi-linearization method for solving uncoupled Van der Pol equation, *J. Anal.*, 2026. https://doi.org/10.1007/s41478-026-01122-9

17. H. Brunner, *Collocation methods for Volterra integral and related functional differential equations*, Cambridge University Press, 2009. https://doi.org/10.1017/CBO9780511543234

18. X. Li, T. Tang, Convergence analysis of Jacobi spectral collocation methods for Abel-Volterra integral equations of second kind, *Front. Math. China*, **7** (2012), 69–84. https://doi.org/10.1007/s11464-012-0170-0

19. F. Fakhar-Izadi, M. Dehghan, An efficient pseudo-spectral Legendre–Galerkin method for solving a nonlinear partial integro-differential equation arising in population dynamics, *Math. Methods Appl. Sci.*, **36** (2013), 1485–1511. https://doi.org/10.1002/mma.2698

20. B. Shiri, D. Baleanu, All linear fractional derivatives with power functions' convolution kernel and interpolation properties, *Chaos Solitons Fractals*, **170** (2023), 113399. https://doi.org/10.1016/j.chaos.2023.113399

21. S. S. Motsa, V. M. Magagula, P. Sibanda, A bivariate Chebyshev spectral collocation quasilinearization method for nonlinear evolution parabolic equations, *Sci. World J.*, **2014** (2014), 581987. https://doi.org/10.1155/2014/581987

22. S. Syedzagiriya, Efficient computational approaches for solving integro-differential equations in engineering applications, *Front. Math. Comput. Res.*, 2026, 26–34.

23. J. C. Mason, D. C. Handscomb, *Chebyshev polynomials*, New York: Chapman and Hall/CRC, 2002. https://doi.org/10.1201/9781420036114

24. S. U. Khan, M. Ali, I. Ali, A spectral collocation method for stochastic Volterra integro-differential equations and its error analysis, *Adv. Differ. Equ.*, **2019** (2019), 161. https://doi.org/10.1186/s13662-019-2096-2

25. T. K. Yuldashev, F. D. Rakhmonov, Nonlocal problem for a nonlinear fractional mixed type integro-differential equation with spectral parameters, *AIP Conf. Proc.*, **2365** (2021), 060003. https://doi.org/10.1063/5.0057147

26. A. Atangana, Z. Hammouch, Fractional calculus with power law: The cradle of our ancestors, *Eur. Phys. J. Plus*, **134** (2019), 429. https://doi.org/10.1140/epjp/i2019-12777-8

27. C. Canuto, M. Y. Hussaini, A. Quarteroni, T. A. Zang, *Spectral methods: Fundamentals in single domains*, Berlin, Heidelberg: Springer, 2006. https://doi.org/10.1007/978-3-540-30726-6

28. J. Shen, T. Tang, L. L. Wang, Spectral methods: Algorithms, analysis and applications, Berlin, Heidelberg: Springer, 2011. https://doi.org/10.1007/978-3-540-71041-7

29. D. L. Marchisio, J. T. Pikturna, R. O. Fox, R. D. Vigil, A. A. Barresi, Quadrature method of moments for population-balance equations, *AIChE J.*, **49** (2003), 1266–1276. https://doi.org/10.1002/aic.690490517

30. M. Samuel, S. S. Motsa, *Computational and numerical analysis of differential equations using spectral based collocation method*, PhD Thesis, University of KwaZulu-Natal, 2019.

31. Z. Ma, C. Huang, An hp-version fractional collocation method for Volterra integro-differential equations with weakly singular kernels, *Numer. Algor.*, **92** (2023), 2377–2404. https://doi.org/10.1007/s11075-022-01394-9

32. X. Dai, A. Xiao, W. Bu, Stochastic fractional integro-differential equations with weakly singular kernels: Well-posedness and Euler–Maruyama approximation, *arXiv preprint*, 2019, arXiv:1901.10333. https://doi.org/10.48550/arXiv.1901.10333

33. K. Sadri, D. Amilo, K. Hosseini, E. Hinçal, A. R. Seadawy, A tau-Gegenbauer spectral approach for systems of fractional integro-differential equations with the error analysis, *AIMS Math.*, **9** (2024), 3850–3880. https://doi.org/10.3934/math.2024190